Geochemistry, Geophysics, Geosystems

Supporting Information for

En-echelon rifting and melt in the Comoros

P. Boymond1*, N. Feuillet1*, I. Thinon2*, L. Scholtès3, S. Zaragosi4, S. Leroy5, A. Lemoine2

1Université Paris Cité, Institut de Physique du Globe de Paris (IPGP), France.

2Bureau de Recherches Géologiques et Minières (BRGM), France.

3Université Clermont Auvergne, CNRS, IRD, OPGC, Laboratoire Magmas et Volcans (LMV), France.

4Université de Bordeaux, CNRS, EPOC, UPHE, UMR 5805, France.

5Sorbonne Université, CNRS-INSU, Institut de Sciences de la Terre de Paris, ISTeP, France.

*Corresponding author: Pierre Boymond (boymond@ipgp.fr), Nathalie Feuillet (feuillet@ipgp.fr) , Isabelle Thinon (i.thinon@brgm.fr)
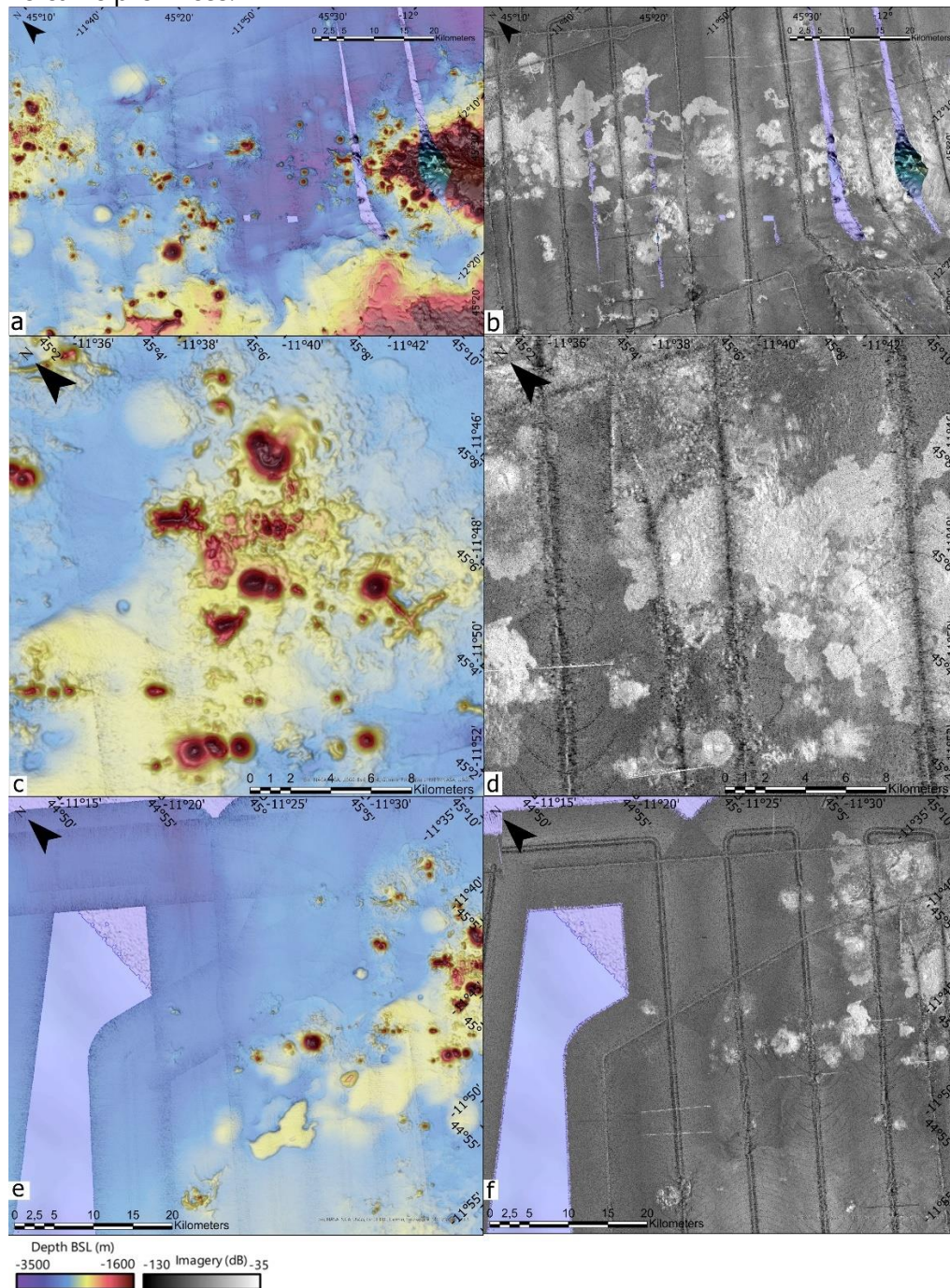
Contents of this file

Supplementary Material 8
Figure S8.1 to S8.4
Table S8.1 to S8.2
Text S8

**Supplementary material 1:** Bathymetry and backscatter maps in Mwezi and N'Droundé volcanic provinces.

Figure S1-1. a, c, e : SISMAORE high-resolution MBES Bathymetry (superimposed to slope gradients). b, d, f : backscatter mosaic map of the three morphologically distinct subarea of the Mwezi volcanic field: M1 (a, b), M2 (c, d) and M3 (e, f). In Background

(transparent layer) : bathymetry from Tzevaritzian et al. (2021) and @GEBCO doi:10.5285/e0f0bb80-ab44-2739-e053-6c86abc0289c).
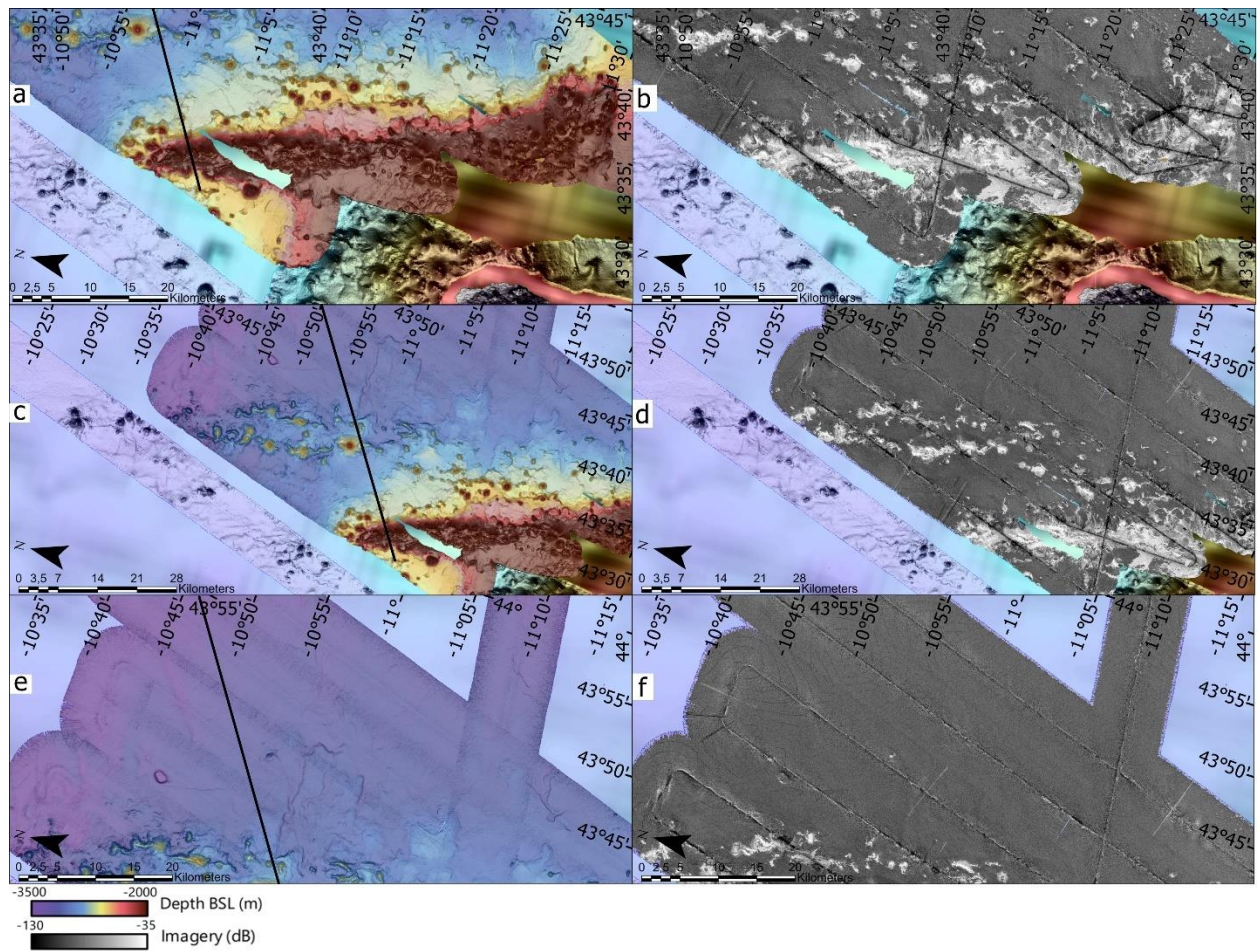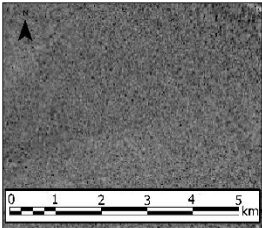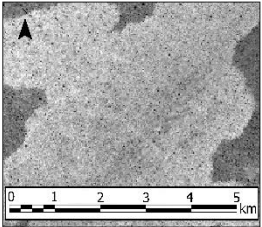
Figure S1-2. a, c, e : SISMAORE high-resolution MBES Bathymetry (superimposed to slope gradients) . b, d, f: backscatter mosaic maps of the three morphologically distinct subareas of the N'Drounde volcanic field : N1 (a, b), N2 (c, d) and N3 (e, f). Background: bathymetry as in Figure S1-1).
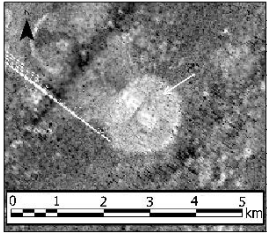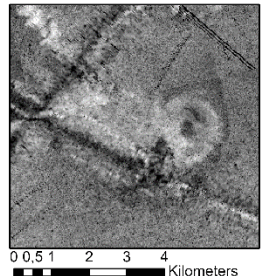
Supplementary material 2: Backscatter facies of a large set of lava flows in the Mwezi province

Geochemistry, Geophysics, Geosystems
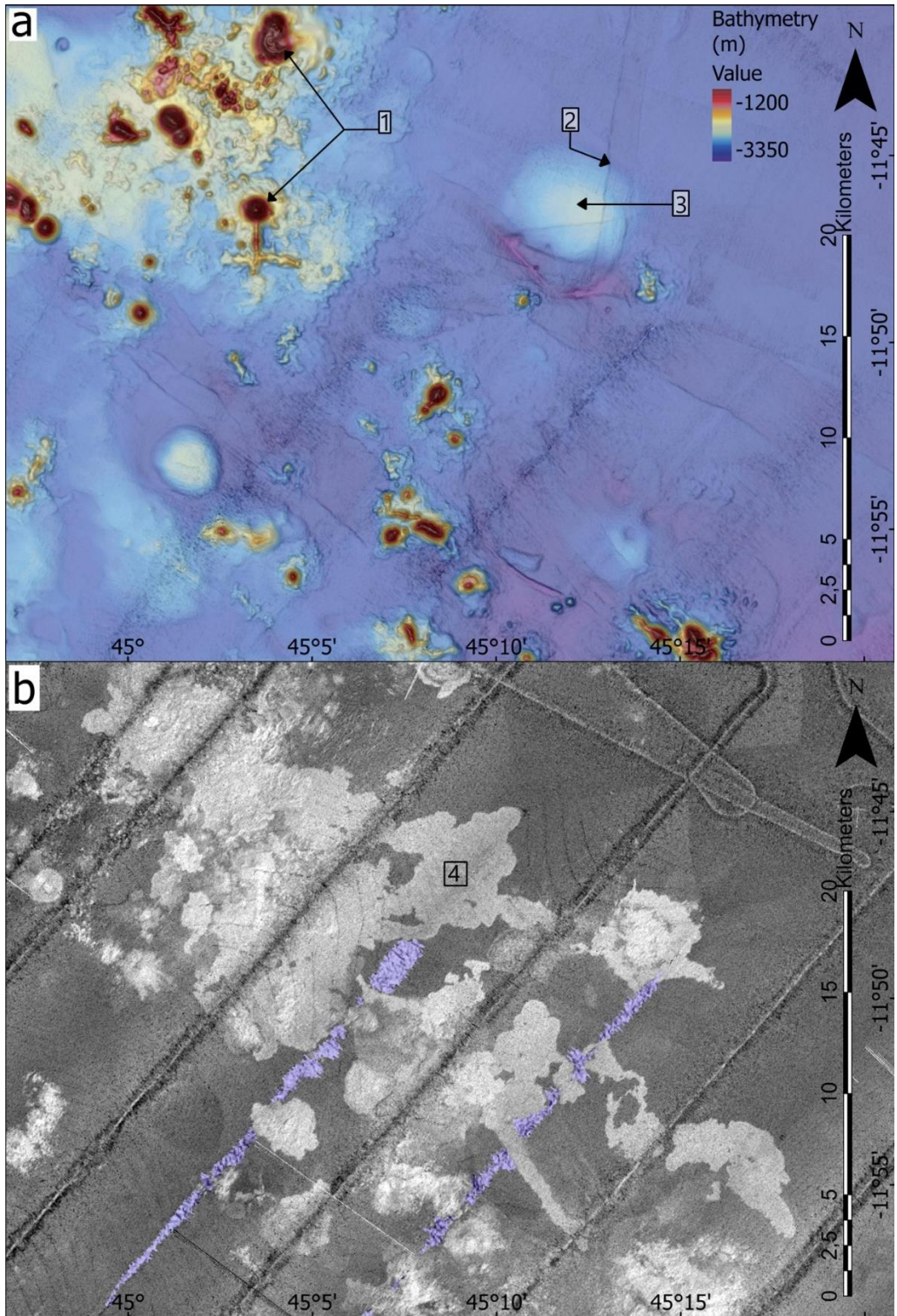
Figure S2-1. a) SISMAORE High-Resolution MBES Bathymetry (superimposed to slope gradients) straddling the Subareas M1-M2 in the Mwezi volcanic province and b) backscatter mosaic maps. Number 1: volcanic edifices, 2: normal fault scarps, 3: forced folds, 4: the lava flows.
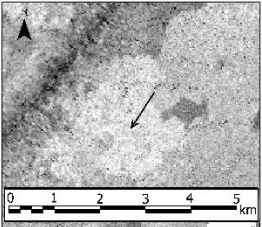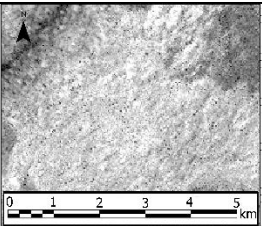
Table S2-1. Backscatter facies of the seafloor.

Facies	Names and colors of reflective facies on maps of Fig. S2-2	Backscatter maps	Description	Interpretation/ setting
Low reflectivity	B1		Homogeneous	Loose sediments on the flat seafloor / Abyssal plain
Medium reflectivity	B2		Homogeneous	Rocky seafloor Lava-flows (covered or not by a thin sediment layer) / around seamount
High reflectivity	B3		Heterogeneous with patches	Rocky seafloor Lava-flows (Outcropping rocks, no cover or not by a very thin sediment layer) / around the seamounts
High to very high reflectivity	B4		Heterogeneous with N45 striations	Rocky seafloor (Outcropping rocks, not covered by sediments) /Lava-flows around the seamounts

6

	B5		Homogeneous	Rocky seafloor (Outcropping rocks, no covered by sediments) / Volcanic seamounts
Medium reflectivity	B6		Homogeneous	Outcropping rocks, covered by sediments / Volcanic seamounts
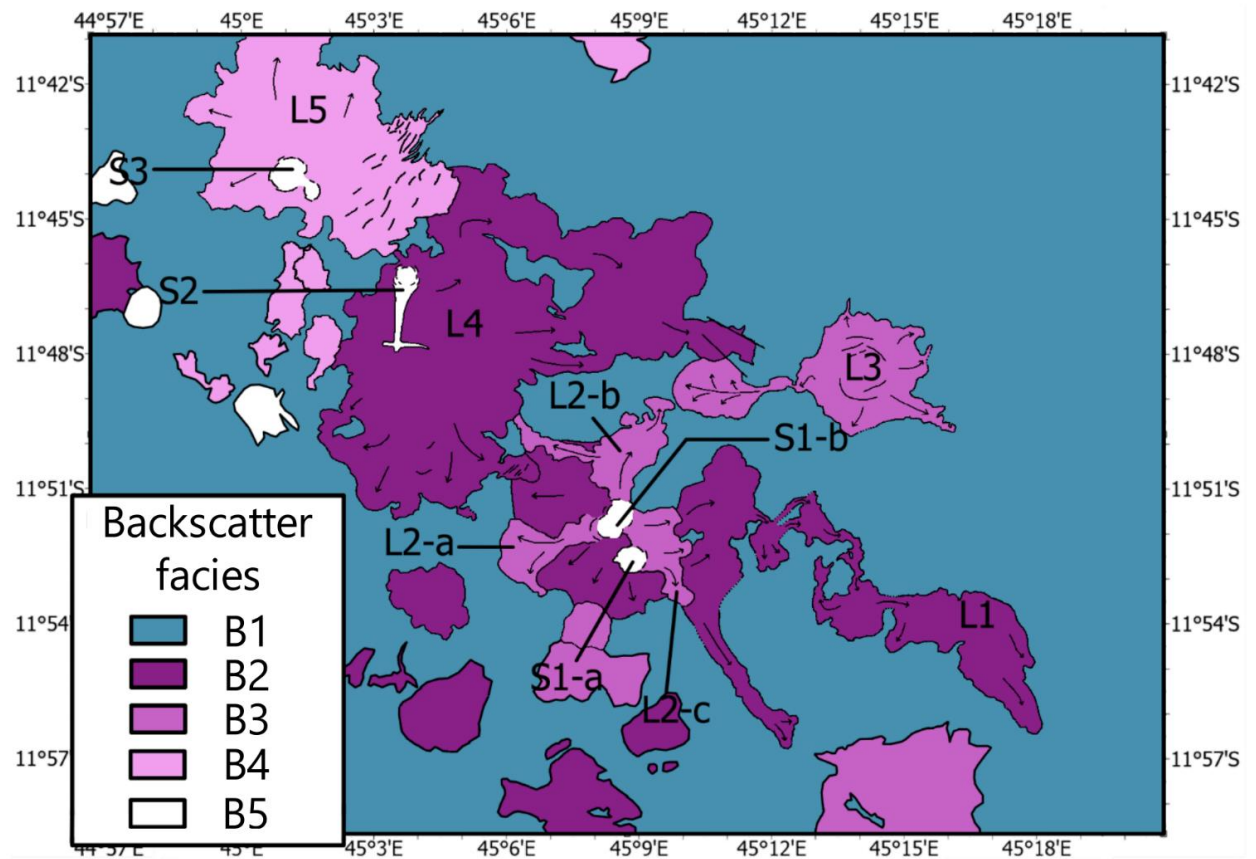
Figure 2: S2-2: Backscatter facies map of a part of the Mwezi province (subarea M1-M2). Facies as in Table S2-1. L1 to L4 : Lava flows, S1, S2, S3: seamounts. Black arrows: inferred direction of lava flows.

Supplementary material 3: SISMAORE 48-Channel reflection seismic data (location and uninterpreted profiles).
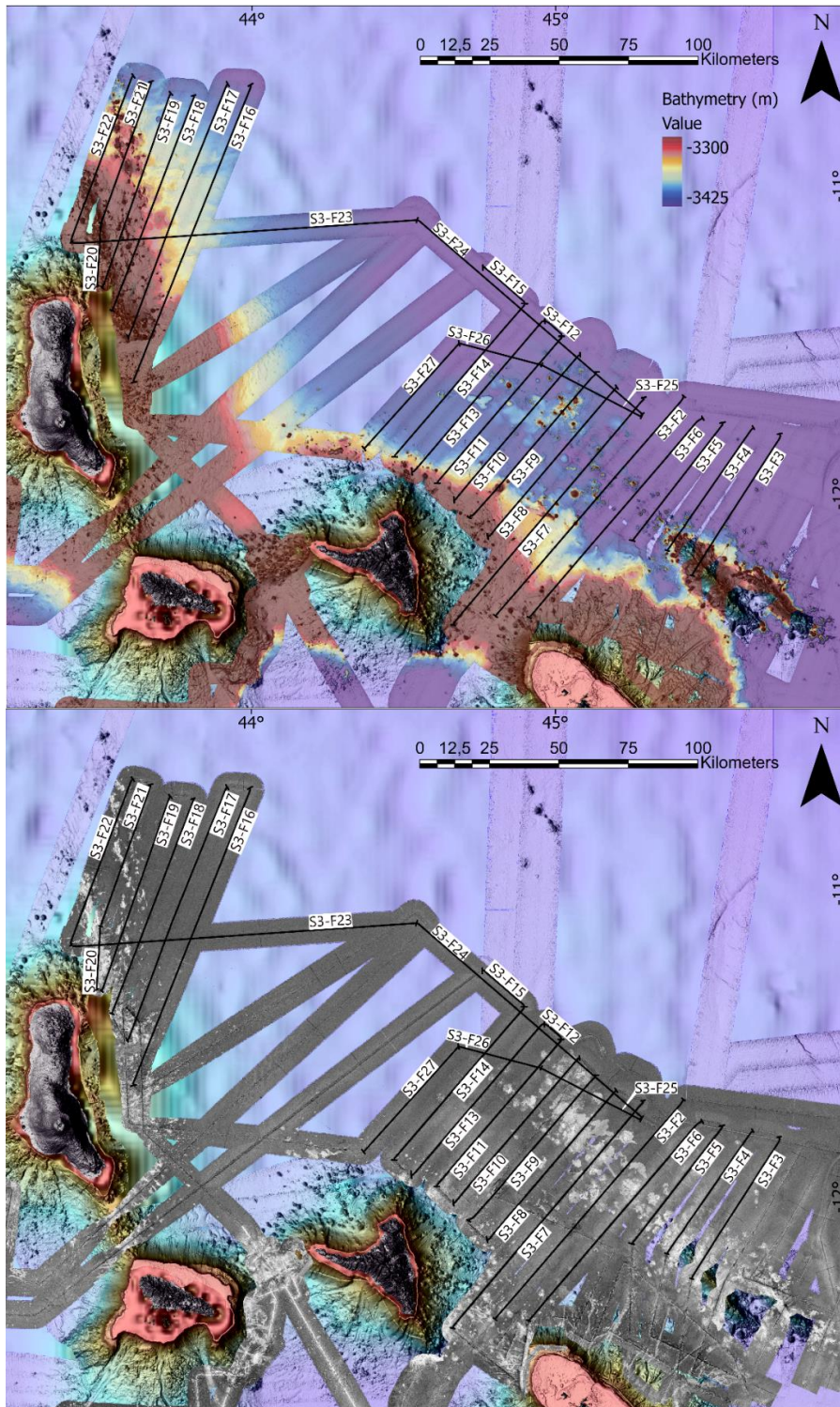
Figure S3-1: Routes of the SISMAORE 48-channel seismic profiles superimposed on a) bathymetric and topographic map. Bathymetry with slope gradients as in Figures S1-1,

topography from GEBCO_2022 (doi:10.5285/e0f0bb80-ab44-2739-e053-6c86abc0289c) data, b) superimposed on backscatter data; background bathymetry as in Figure S1-1. The names of the figures in which they are presented are in white rectangular boxes along the profiles.
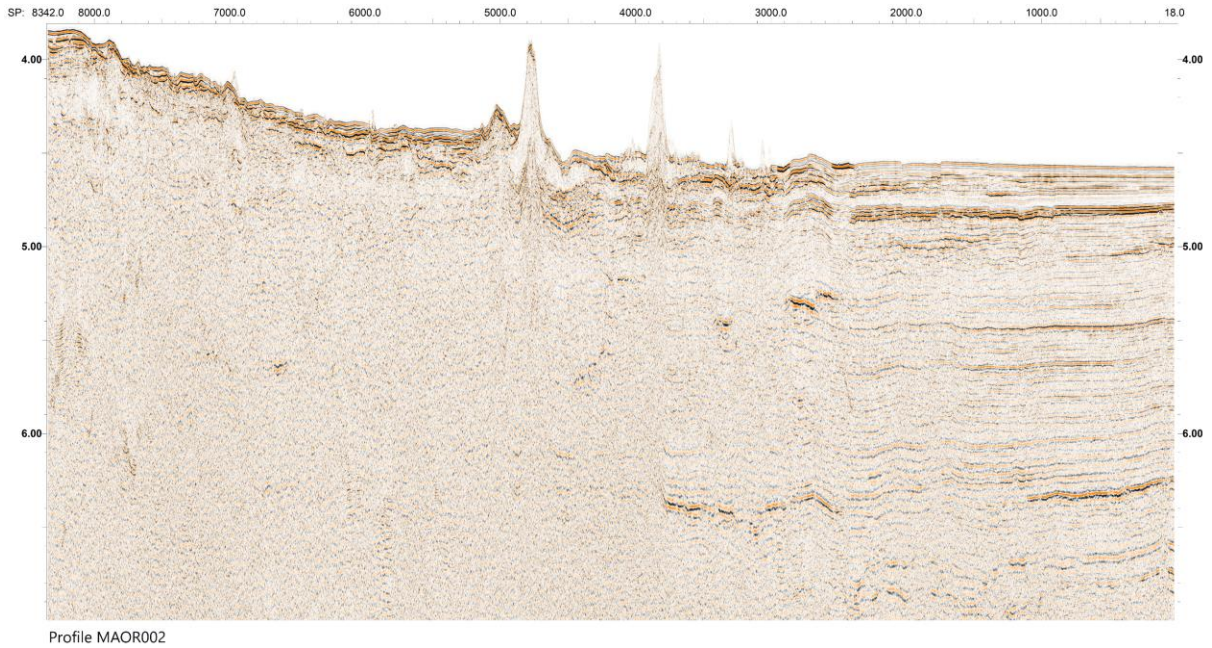
Profile MAOR002

Figure S3-2: Uninterpreted seismic profile MAOR002. X-axis: Common Depth points (CDP) numbers (A CDP interval=12.5 m), Y-axis: times in s TWTT (two-way travel time). Location of the profile in Figure S3-1.

Profile MAOR020

Figure S3-3: Uninterpreted seismic profile MAOR020. Legends and units as in Figure S3-2.

Profile MAOR021

Figure S3-4: Uninterpreted seismic profile MAOR021. Legends and units as in Figure S3-2.

10
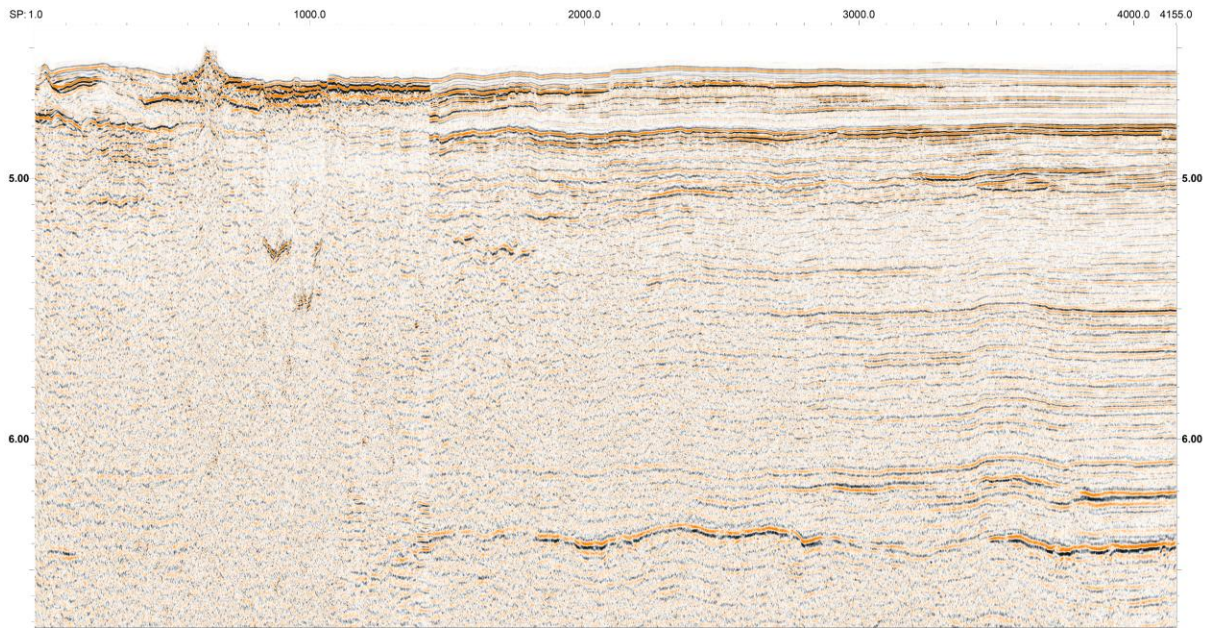
MAOR043

Figure S3-5: Uninterpreted seismic profile MAOR043. Legends and units as in Figure S3-2.

MAOR045

Figure S3-6: Uninterpreted seismic profile MAOR045. Legends and units as in Figure S3-2.

Figure S3-7: Uninterpreted seismic profile MAOR048. Legends and units as in Figure S3-2.

Figure S3-8: Uninterpreted seismic profile MAOR049. Legends and units as in Figure S3-2.

13

Figure S3-9: a) Uninterpreted seismic profile MAOR0051. Legends and units as in Figure S3-2. B, c): interpreted zooms of the profile. Symbols and colors of the sedimentary units, seismic horizons and reflectors, volcanic products and tectonic structures as in figures 6 and 7 of the main text. a) zoom on a volcanic cone emplaced along the border fault (BF). The base of the cone lies below the red seismic horizon Hi2 (1Ma), implying that it

14

emplaced before 1 Ma. b) zoom of the profile showing volcanic cones within the Mwezi-Jumelles rift. The base of the cones lies above the red seismic horizon Hi2 (1Ma), implying that they emplaced after 1 Ma.

Figure S3-10: a) Uninterpreted seismic profile MAOR0052. Legends and units as in Figure S3-2. b) interpreted zoom of the profile. Symbols and colors of the sedimentary units, seismic horizons and reflectors, volcanic products and tectonic structures as in figures 6

and 7 of the main text. The zoom shows in more detail of the network of sills and dyke intrusions as well as recent forced folds and lava flows in the Mwezi volcanic province.
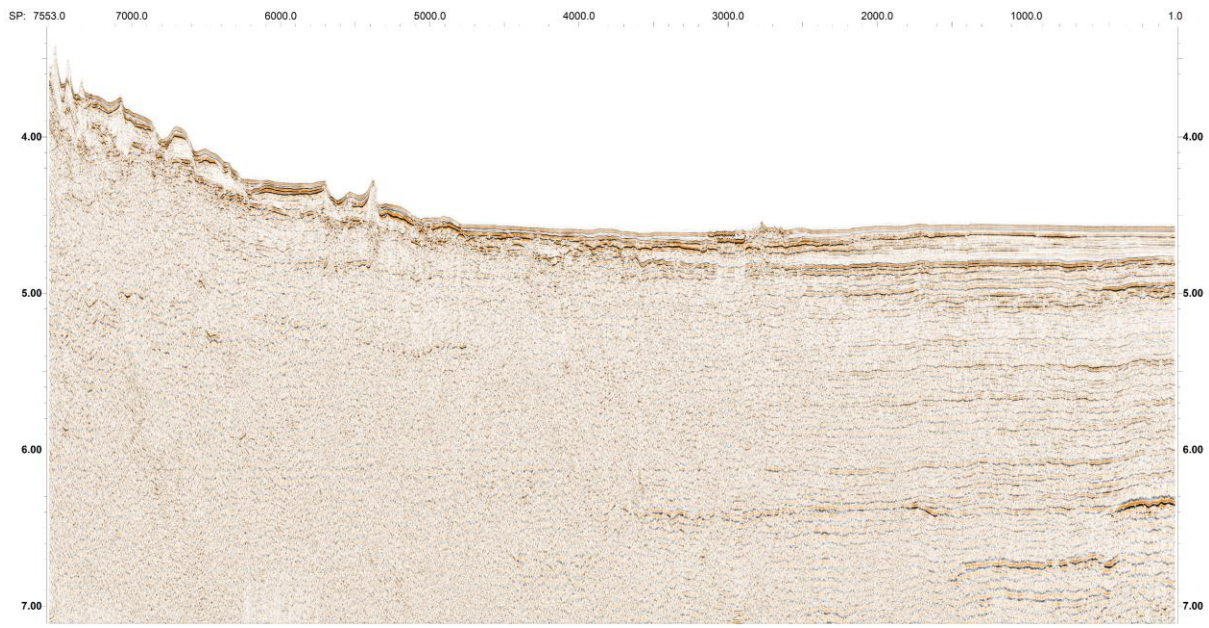

MAOR053

Figure S3-11: Uninterpreted seismic profile MAOR053. Legends and units as in Figure S3-2.

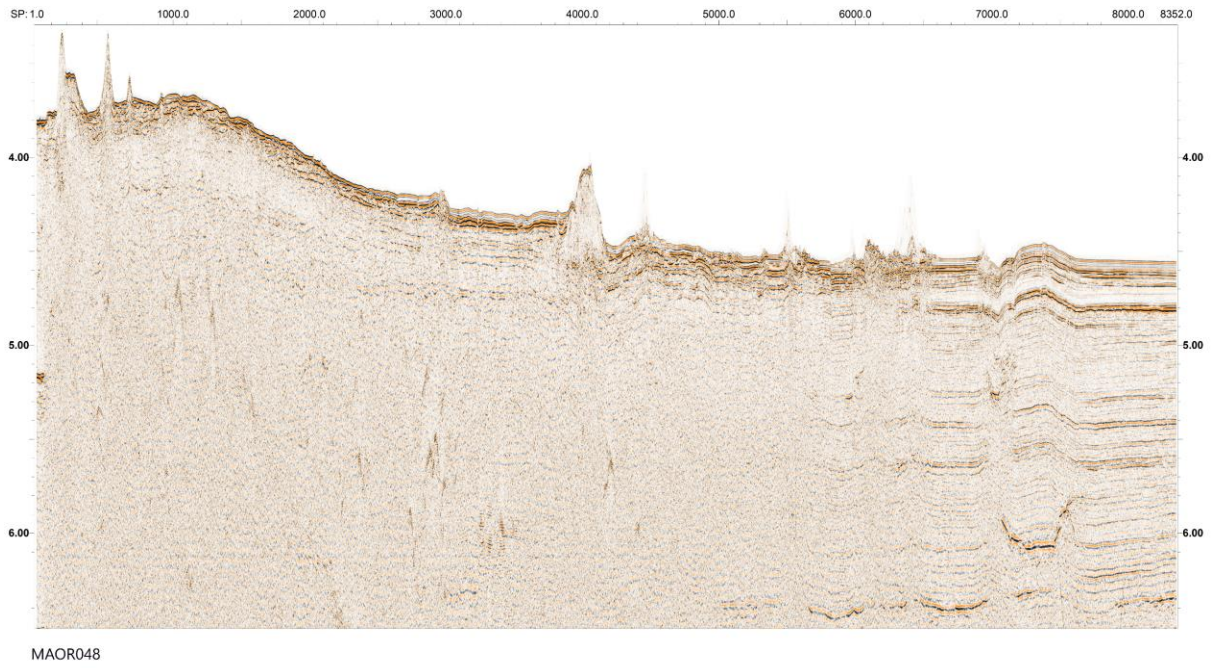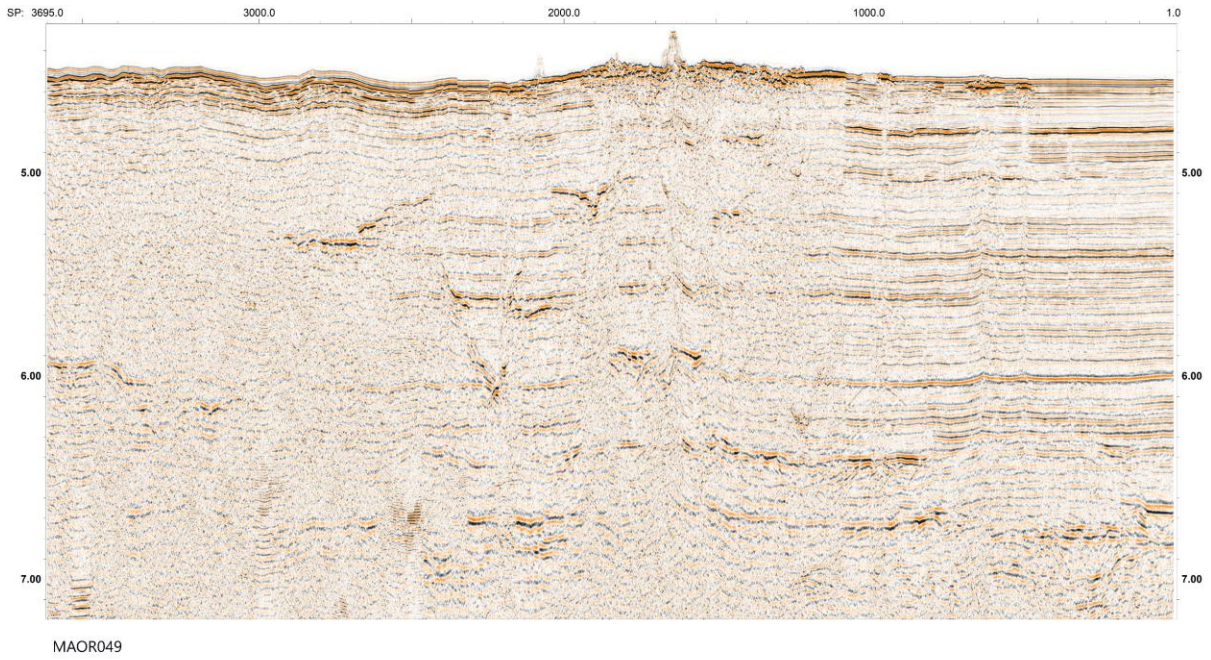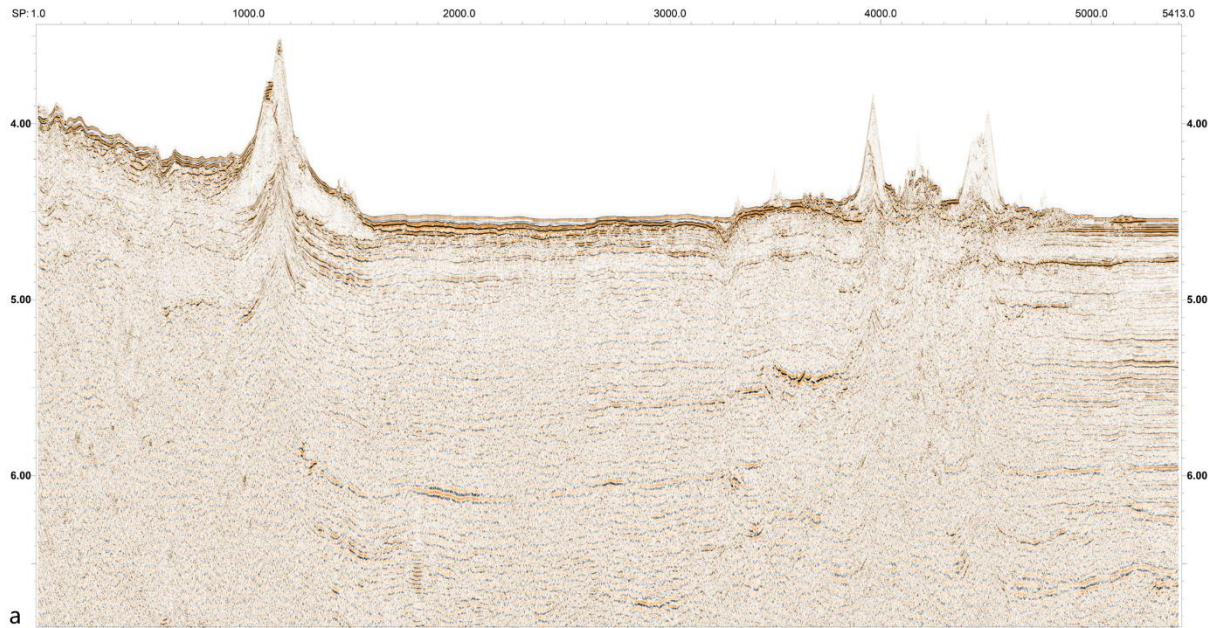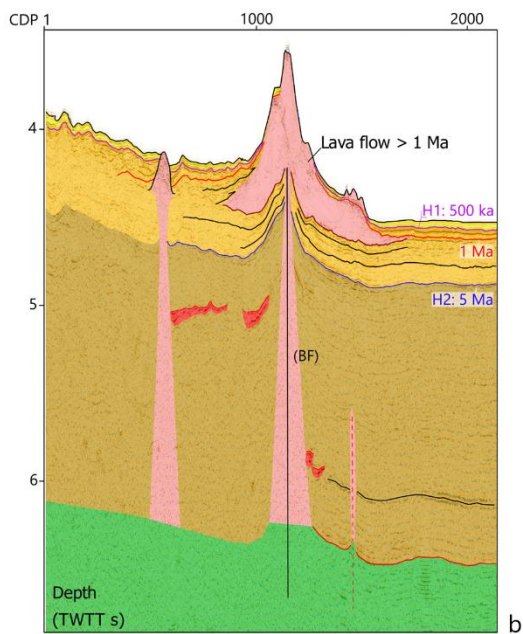**Figure S3-12:** Uninterpreted seismic profile MAOR054. Legends and units as in Figure S3-2.

Figure S3-13: Uninterpreted seismic profile MAOR055. Legends and units as in Figure S3-2.

MAOR056

Figure S3-14: Uninterpreted seismic profile MAOR056. Legends and units as in Figure S3-2.

Figure S3-15: Uninterpreted seismic profile MAOR057. Legends and units as in Figure S3-2.

18

Figure S3-16: Uninterpreted seismic profile MAOR066. Legends and units as in Figure S3-2.

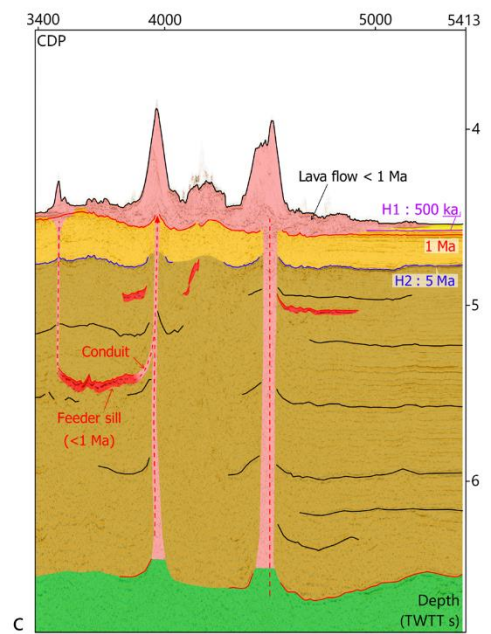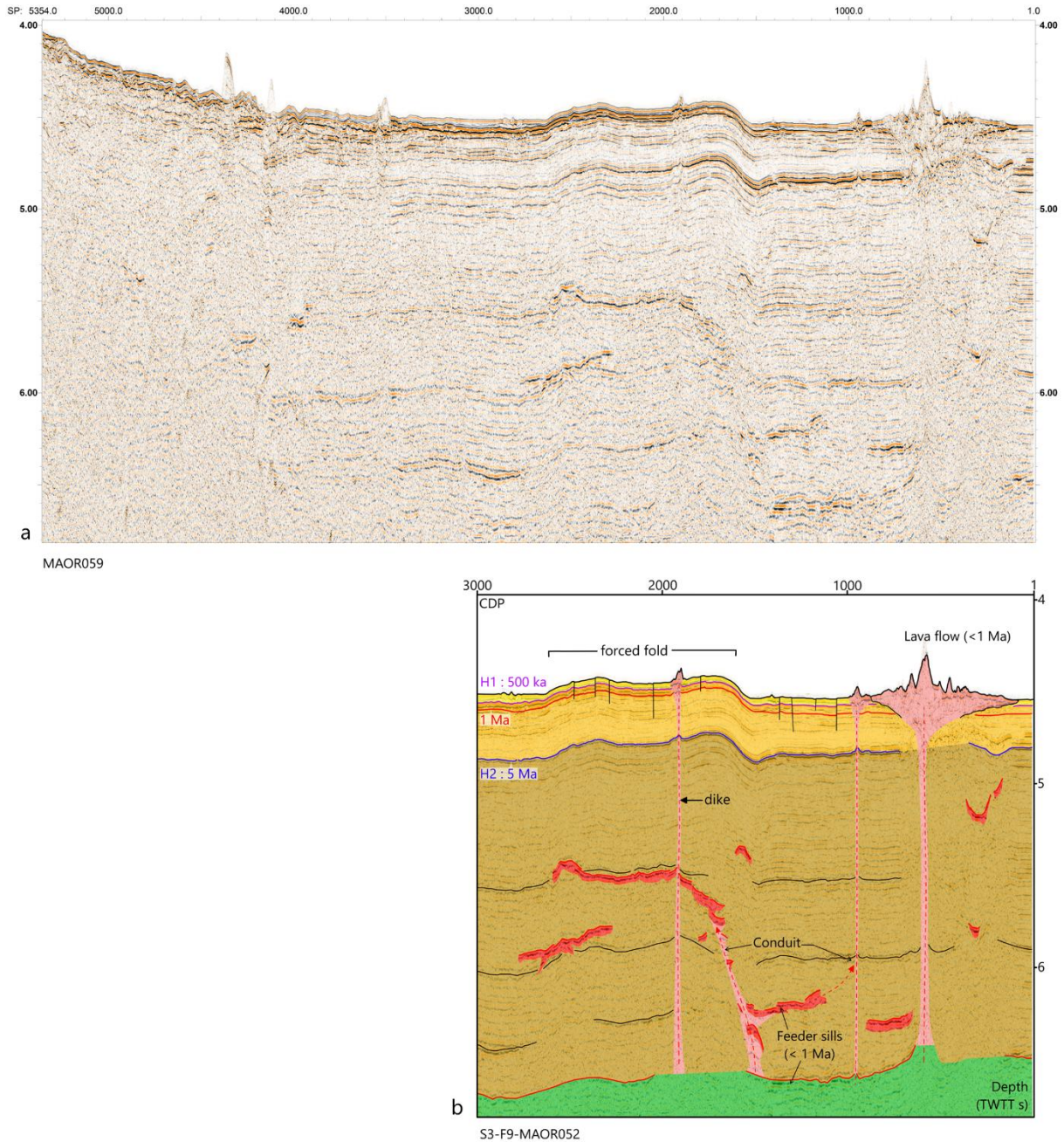**Figure S3-17:** Uninterpreted seismic profile MAOR068. Legends and units as in Figure S3-2.

Figure S3-18: Uninterpreted seismic profile MAOR069. Legends and units as in Figure S3-2.
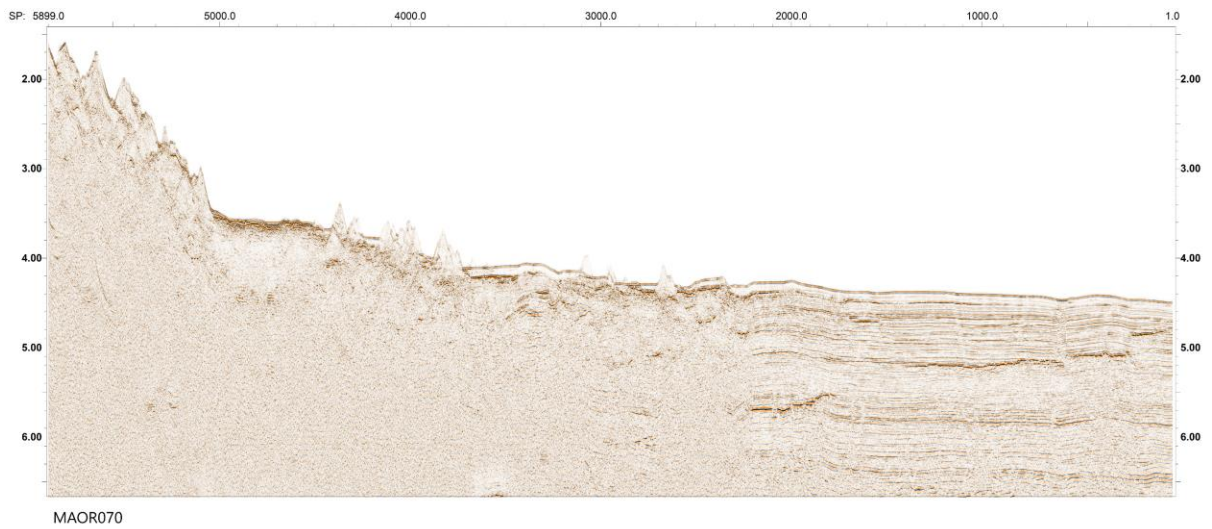
Figure S3-19: Uninterpreted seismic profile MAOR070. Legends and units as in Figure S3-2.
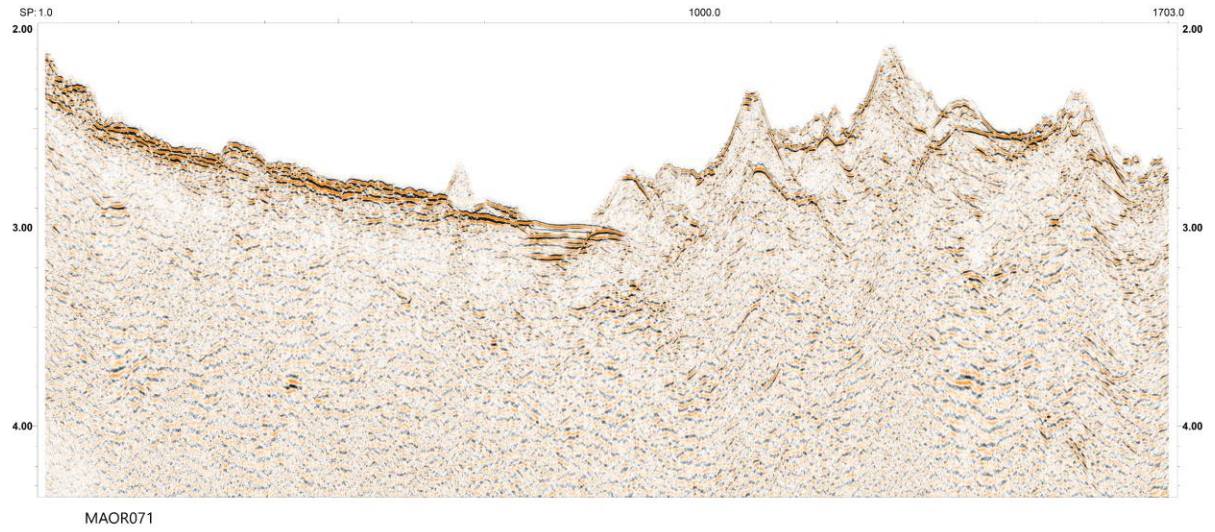
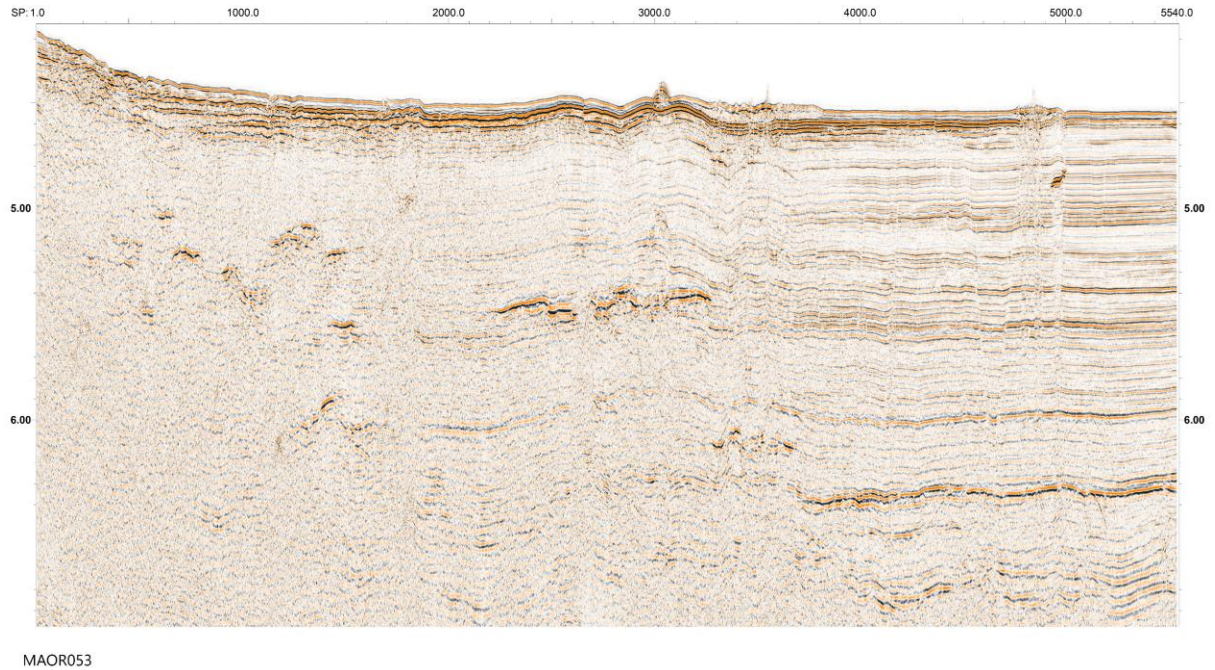**Figure S3-20:** Uninterpreted seismic profile MAOR071. Legends and units as in Figure S3-2.
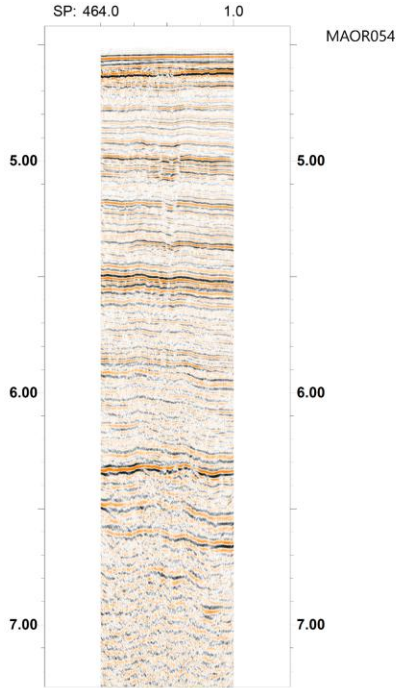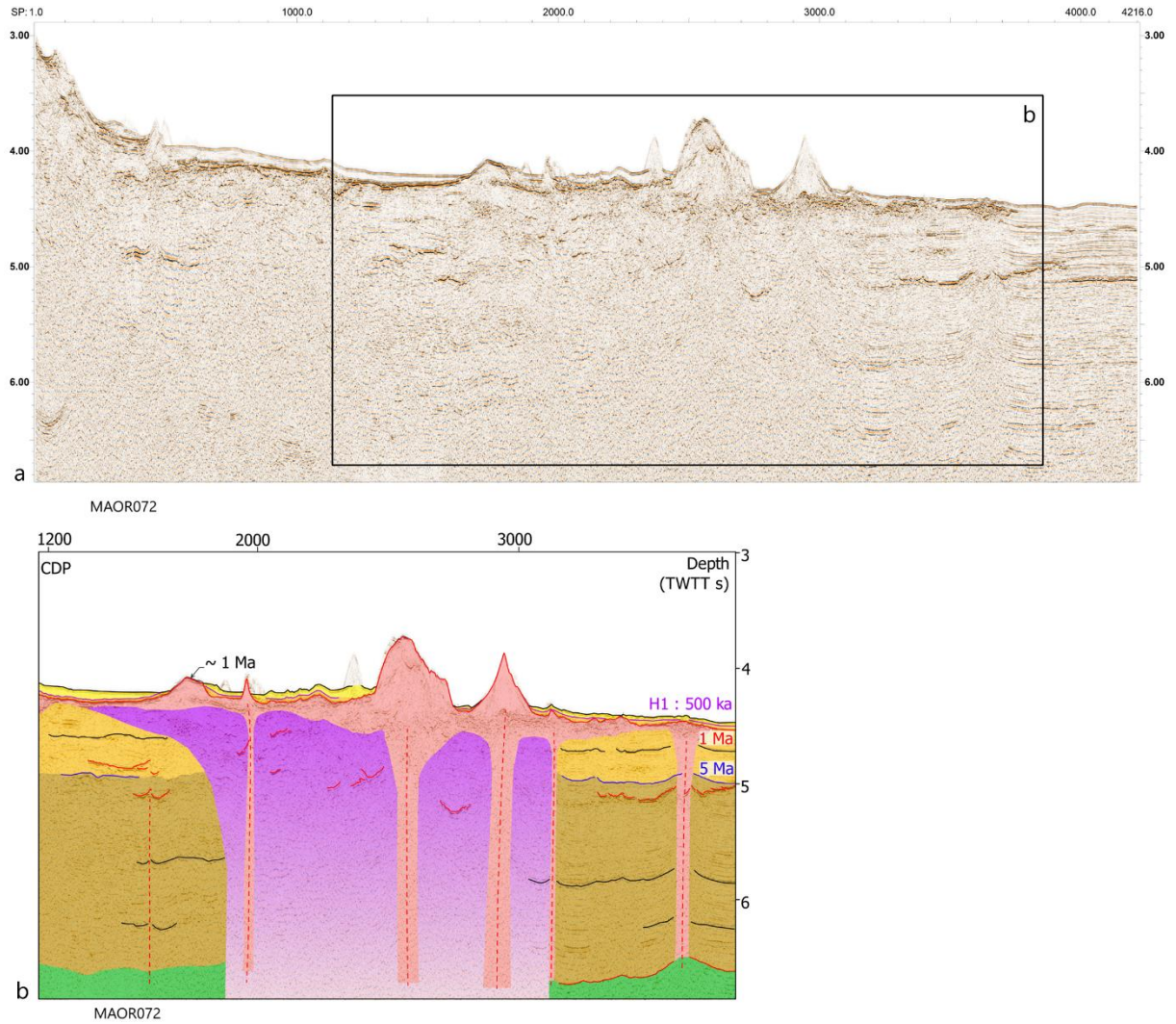
Figure S3-21: a) Uninterpreted seismic profile MAOR072. Legends and units as in Figure S3-2. b) interpreted zoom of the profiles. Symbols and colors of the sedimentary units, seismic horizons and reflectors, volcanic products and tectonic structures as in figures 6 and 7 of the main text. The roots of volcanic edifices and lavas flows are sealed the 1Ma y-Old Hi2 seismic horizon (red color) implying that they emplace prior 1Ma.
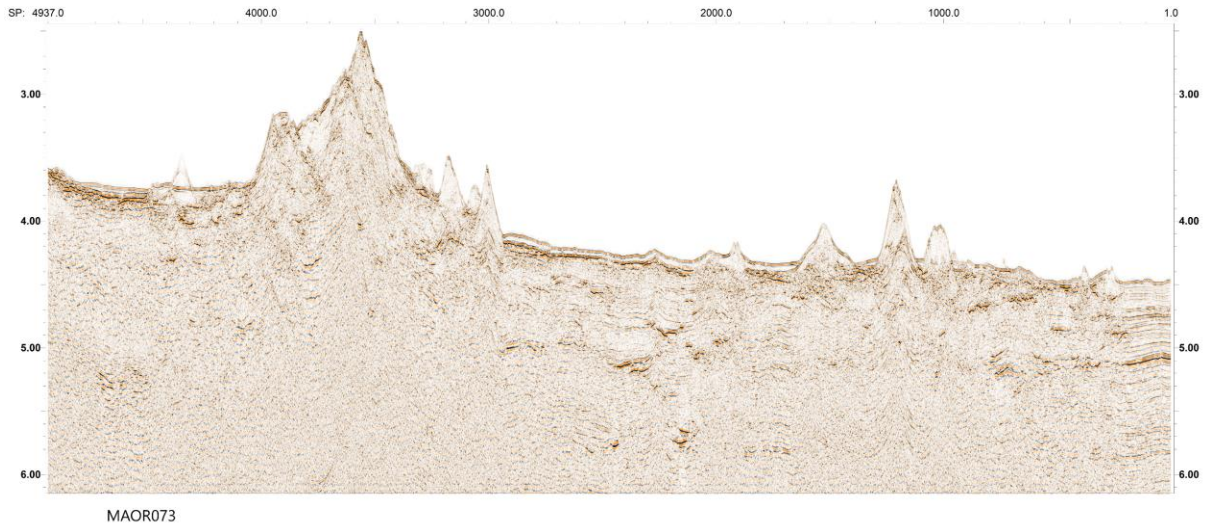
Figure S3-22: Uninterpreted seismic profile MAOR073. Legends and units as in Figure S3-2.
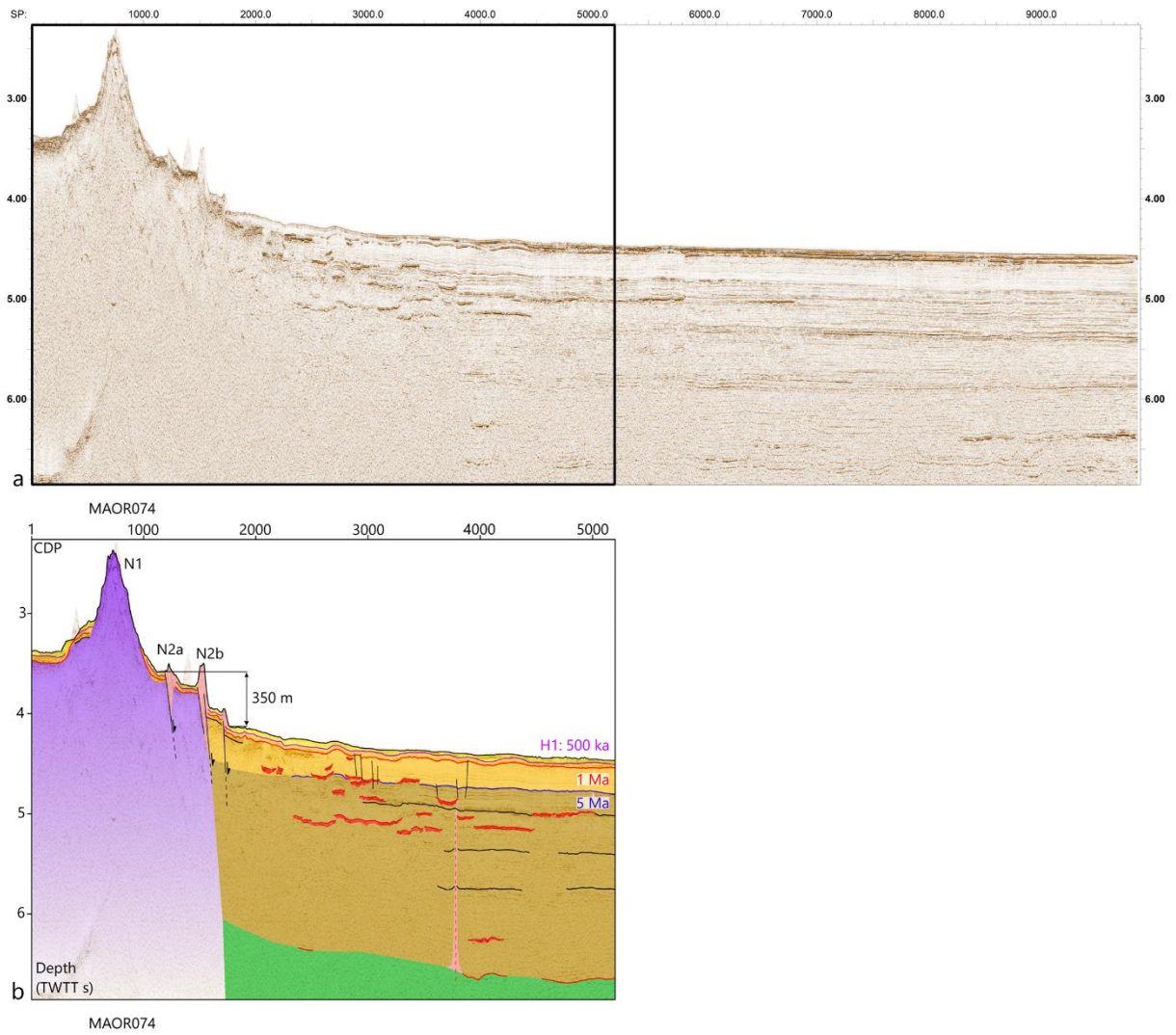
Figure S3-23: a) Uninterpreted seismic profile MAOR074. Legends and units as in Figure S3-2. b) interpreted zoom of the profiles. Symbols and colors of the sedimentary units, seismic horizons and reflectors, volcanic products and tectonic structures as in figures 6 and 7 of the main text.
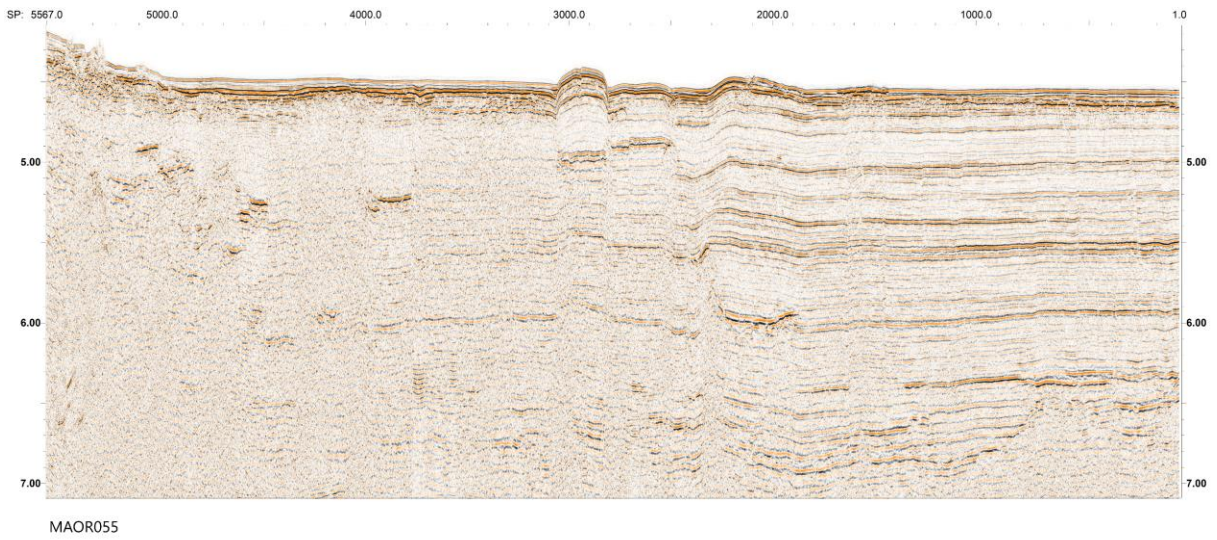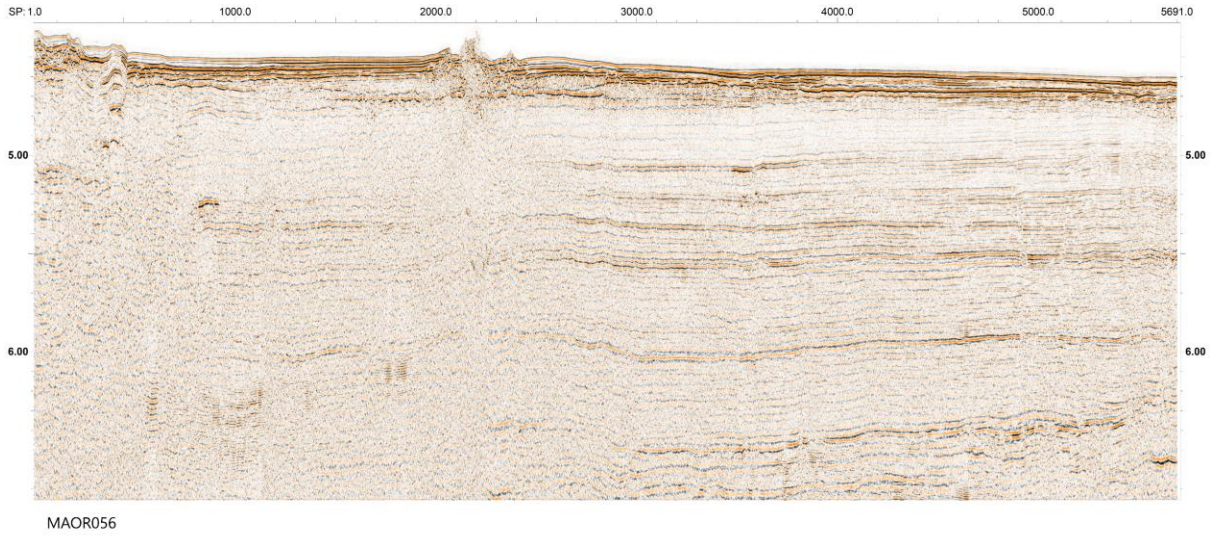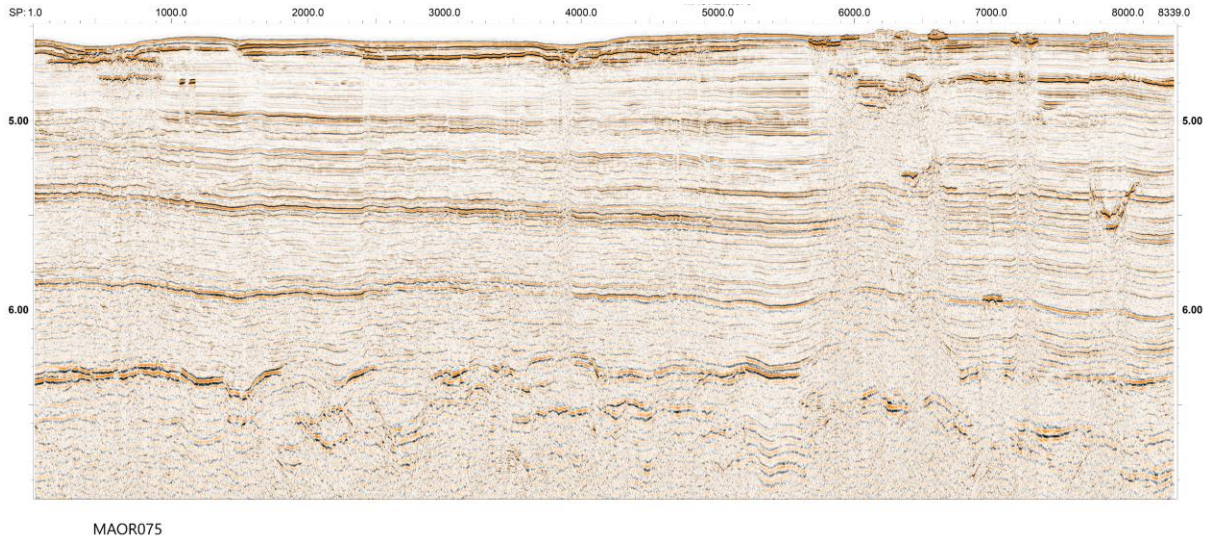
Figure S3-24: Uninterpreted seismic profile MAOR075. Legends and units as in Figure S3-2.

Figure S3-25: Uninterpreted seismic profile MAOR077. Legends and units as in Figure S3-2.
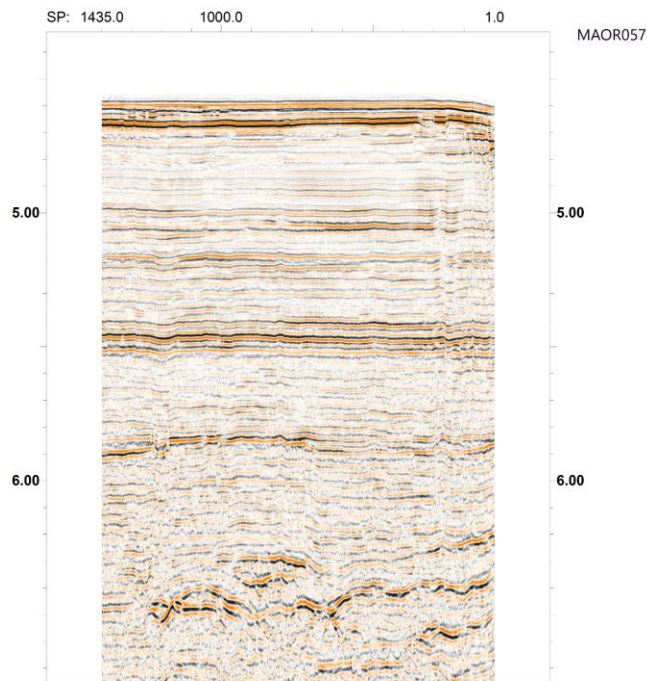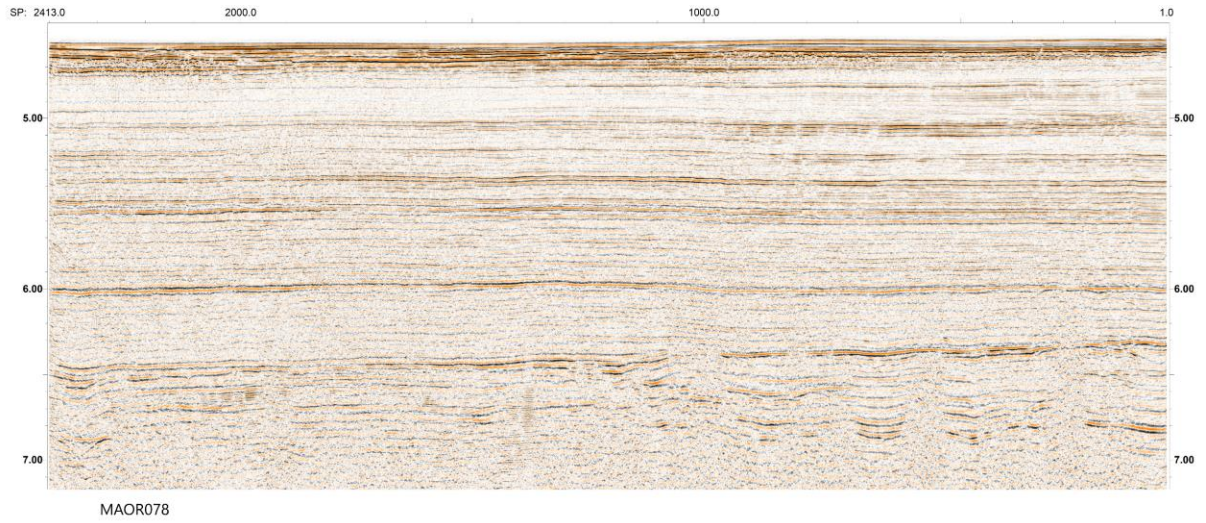
Figure S3-26: Uninterpreted seismic profile MAOR078. Legends and units as in Figure S3-2.

Figure S3-27: Uninterpreted seismic profile MAOR079. Legends and units as in Figure S3-2.

**Supplementary material 4:** SISMAORE sub-bottom profiler data (location and uninterpreted profiles).
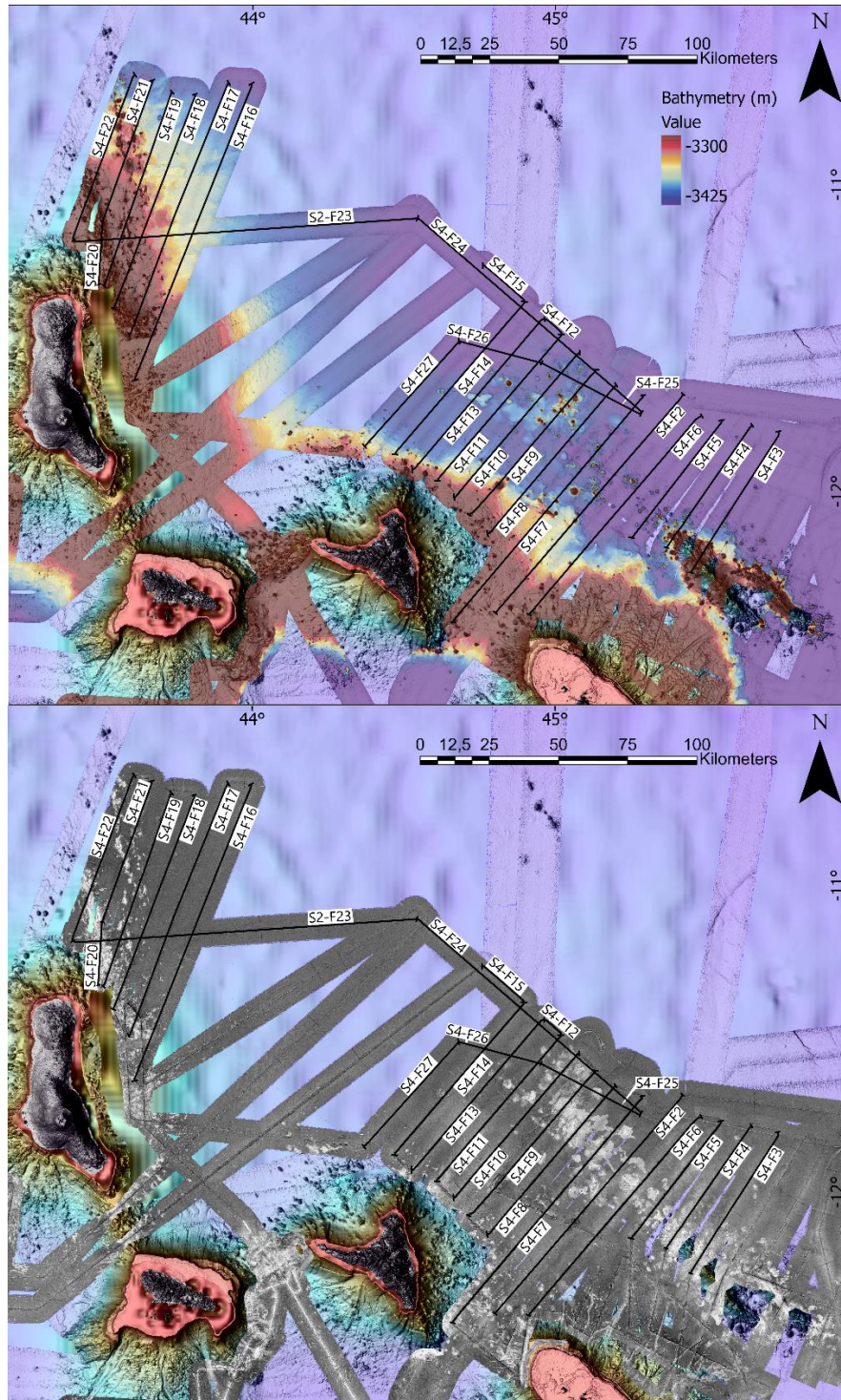
Figure S4-1: Routes of SISMAORE sub-bottom profile (SBP) data superimposed on a) bathymetry with slope gradients as in Figures S1-1, topography from XXXX data, b)

superimposed on backscatter data (background bathymetry as in Figure S1-1. Names of the figures in which they are presented are in white rectangular boxes along the profile.
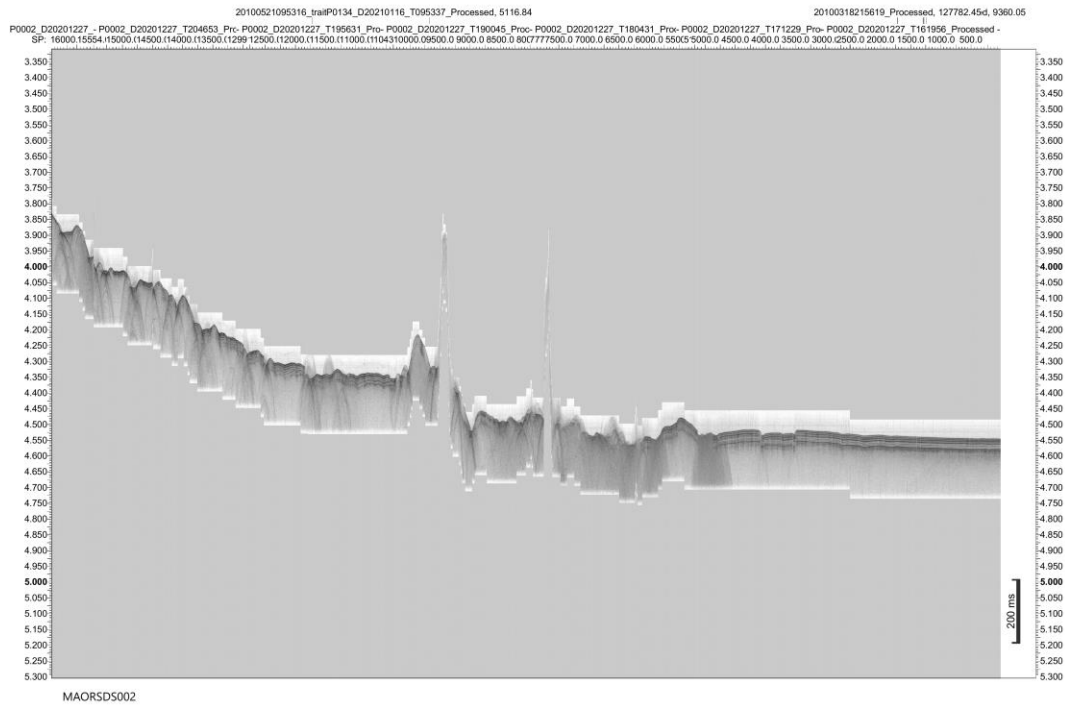
Figure S4-2: SW-NE oriented uninterpreted sub-bottom profiler data (SBP) MAORSDS002. X-Axis: CDPs, Y-Axis: Times TWTT (s)
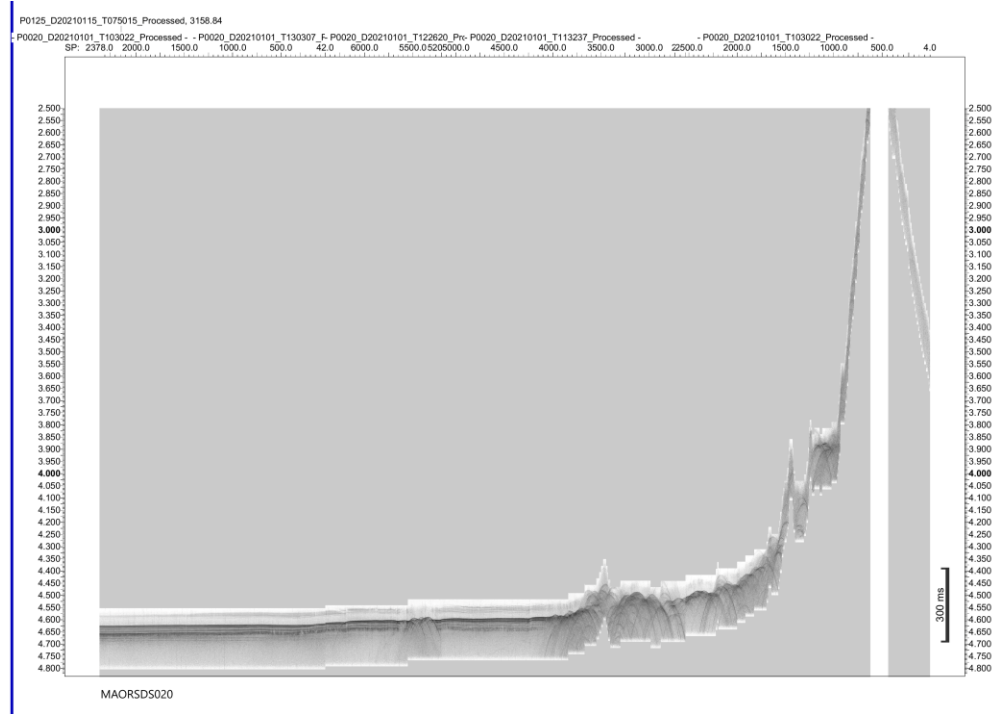
Figure S4-3: NE-SW oriented uninterpreted sub-bottom profiler data (SBP) MAORSDS020. Units as in Figure S4-2.
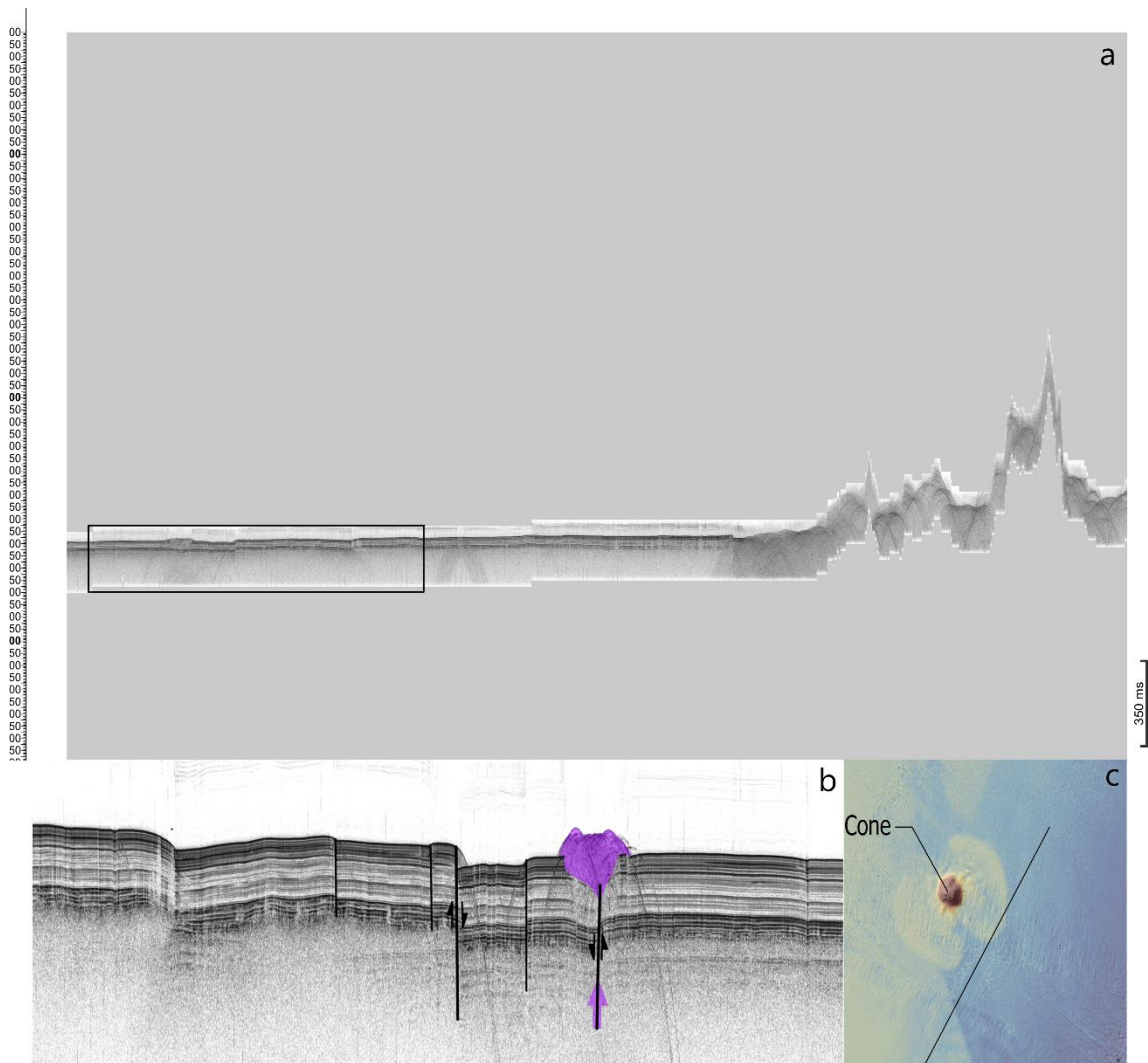
Figure S4-4: a) NE-SW oriented uninterpreted sub-bottom profiler data (SBP) MAORSDS021. Units as in Figure S4-2. b) SW-NE oriented interpreted zoom of a faults-graben system. One of the faults is topped by a lava flow. c) the Graben and the volcanic edifice in the bathymetry. Black line: location of the profile
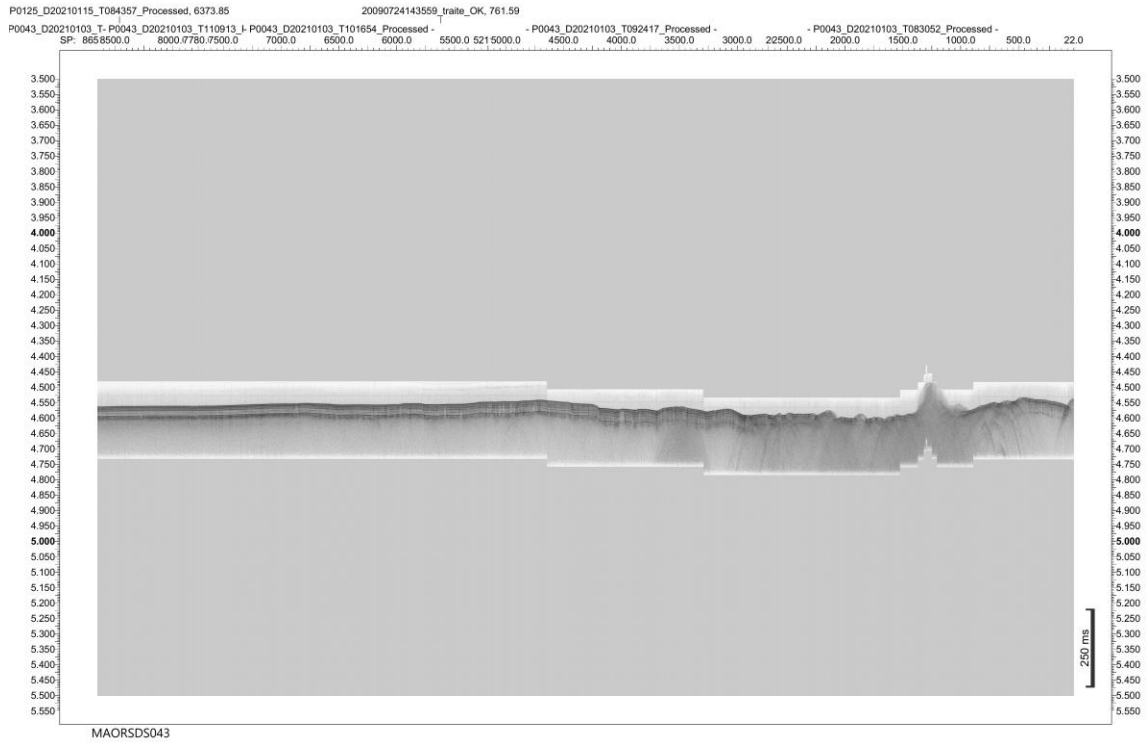
Figure S4-5: NE–SW oriented uninterpreted sub-bottom profiler data (SBP) MAORSDS043. Units as in Figure S4-2.

Figure S4-6: NE-SW oriented uninterpreted sub-bottom profiler data MAORSDS045. Units as in Figure S4-2.

400 ms

Figure S4-7: NE-SW oriented uninterpreted sub-bottom profiler data MAORSDS048. Units as in Figure S4-2.

Figure S4-8: a) NE-SW oriented uninterpreted sub-bottom profiler data MAORSDS049. Units as in Figure S4-2. b) zoom on a volcanic intrusion that might be set along a fault plane.

Figure S4-9: a) NE-SW oriented uninterpreted sub-bottom profiler data MAORSDS051. Units as in Figure S4-2. b) Interpreted zoom on a lava flow (red) sealed by a 200ka old seismic reflector. Symbol and colors as in Figure 8 of the main text. Ages of the sedimentary layers and stratigraphy as in Figure 8 and explanations in the main text.

Figure S4-10: NE-SW oriented uninterpreted sub-bottom profiler data MAORSDS052. Units as in Figure S4-2.

Figure S4-11: NE-SW oriented uninterpreted sub-bottom profiler data MAORSDS053. Units as in Figure S4-2.

Figure S4-12: SE-NW oriented uninterpreted sub-bottom profiler data MAORSDS054. Units as in Figure S4-2.

Figure S4-13: NE-SW oriented uninterpreted sub-bottom profiler data MAORSDS055. Units as in Figure S4-2. Inset: zoom inset showing the recent normal fault system.
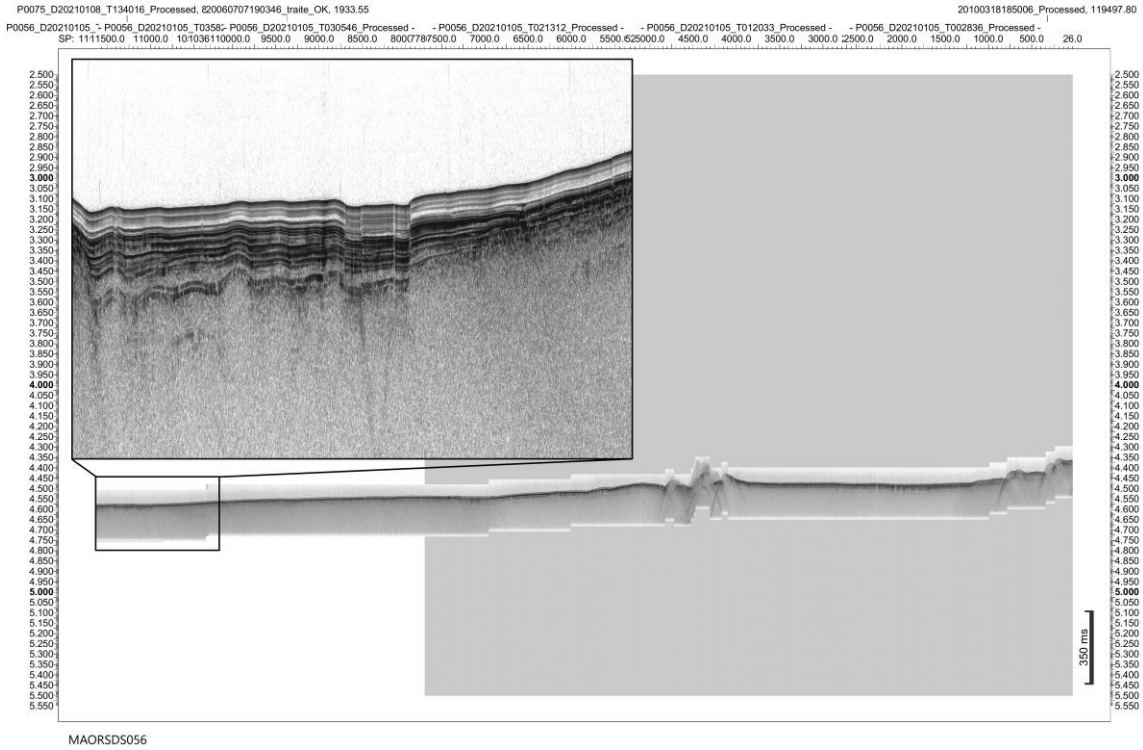
Figure S4-14: NE-SW oriented uninterpreted sub-bottom profiler data. Units as in Figure S4-2. Inset: zoom showing a graben structure.
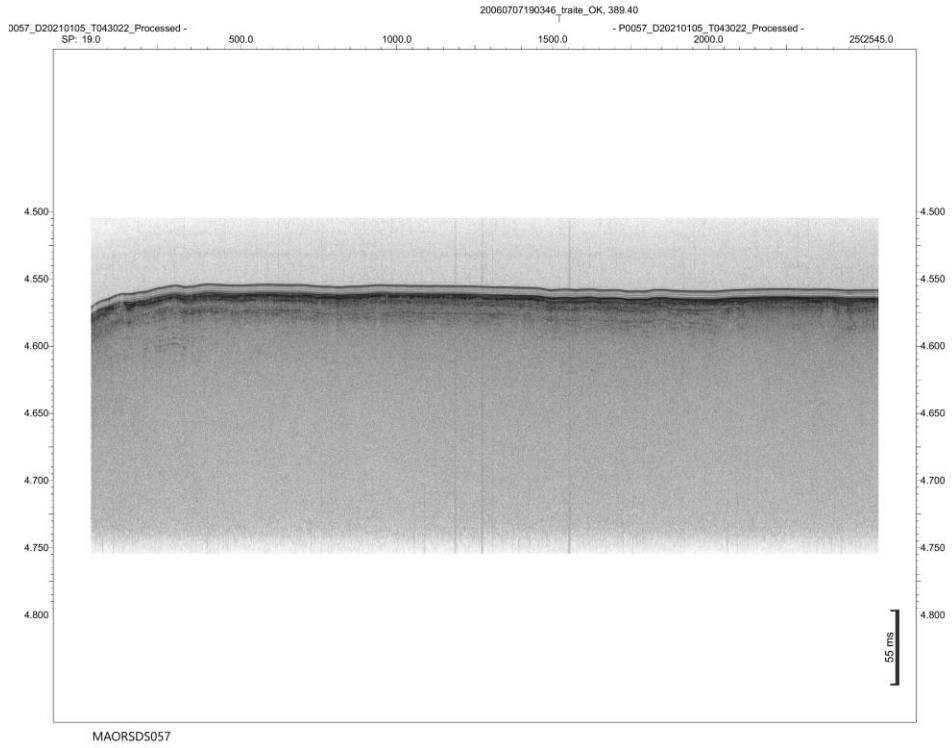
Figure S4-15: SE-NW oriented uninterpreted sub-bottom profiler data MAORSDS057. Units as in Figure S4-2.
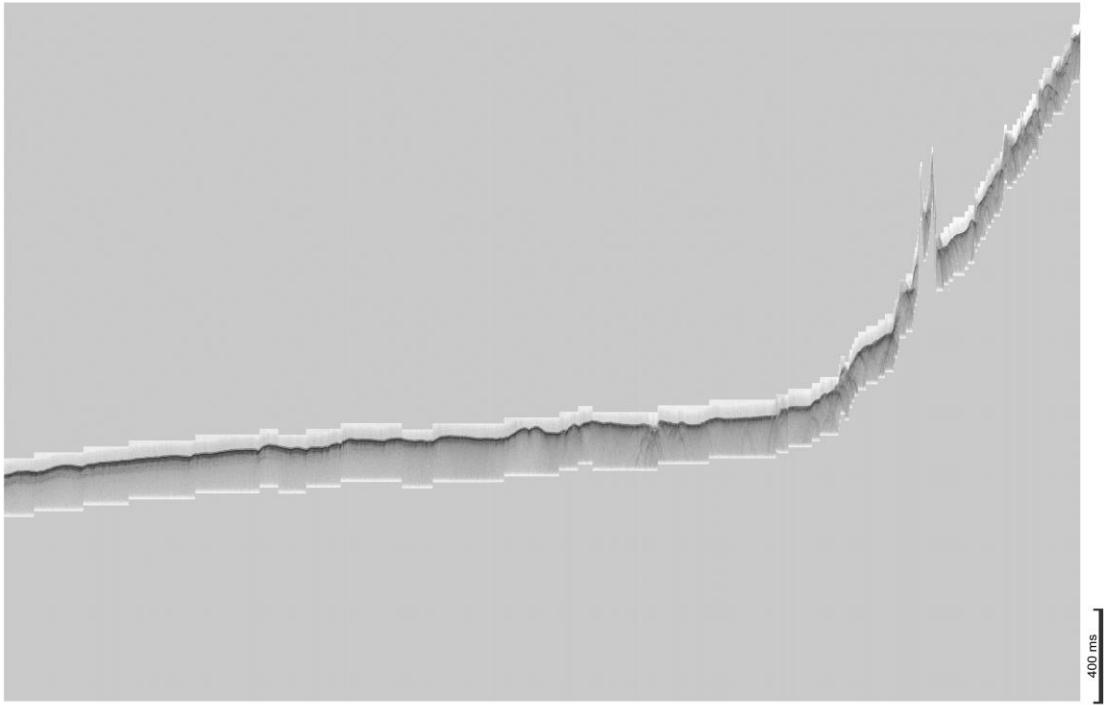
Figure S4-16: NW-SE oriented uninterpreted sub-bottom profiler data MAORSDS066. Units as in Figure S4-2.
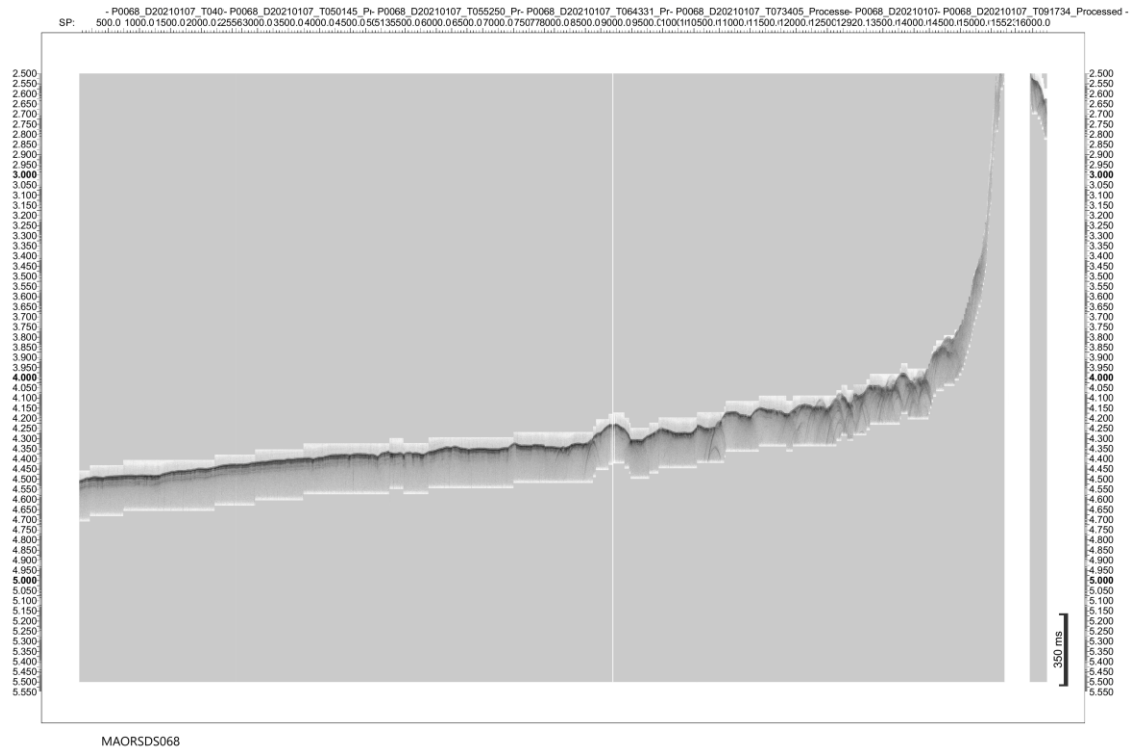
Figure S4-17: NW-SE oriented uninterpreted sub-bottom profiler data MAORSDS068. Units as in Figure S4-2.
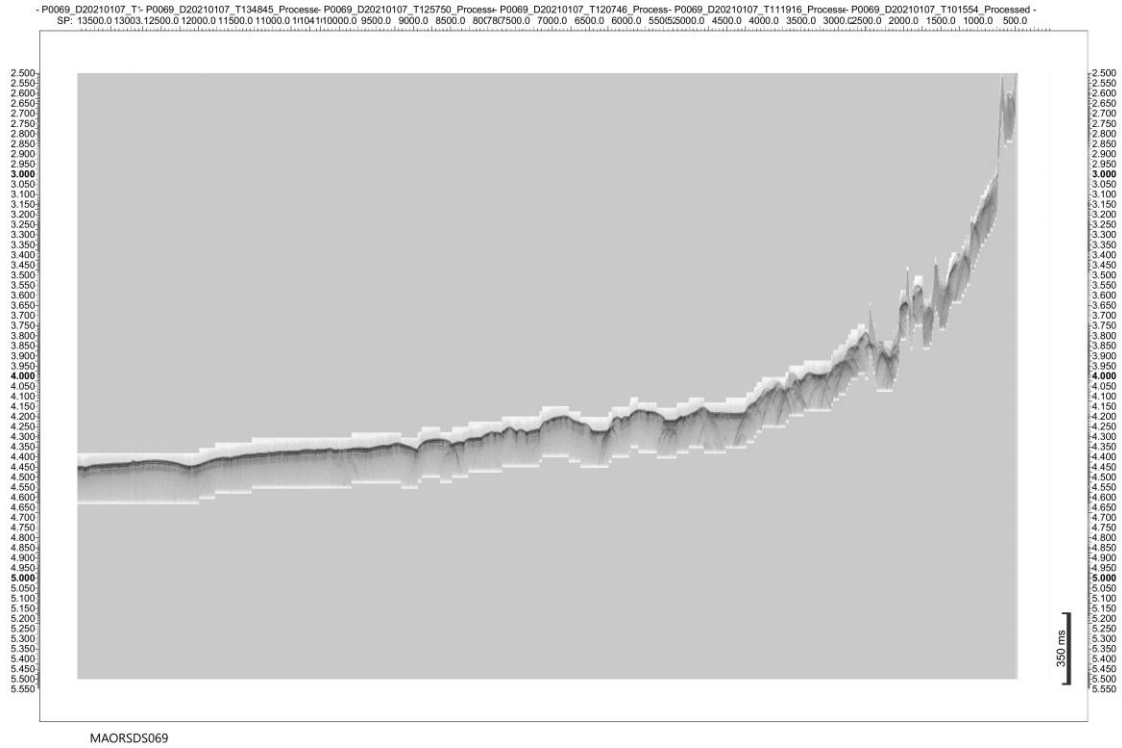
Figure S4-18: NW-SE oriented uninterpreted sub-bottom profiler data MAORSDS069. Units as in Figure S4-2.

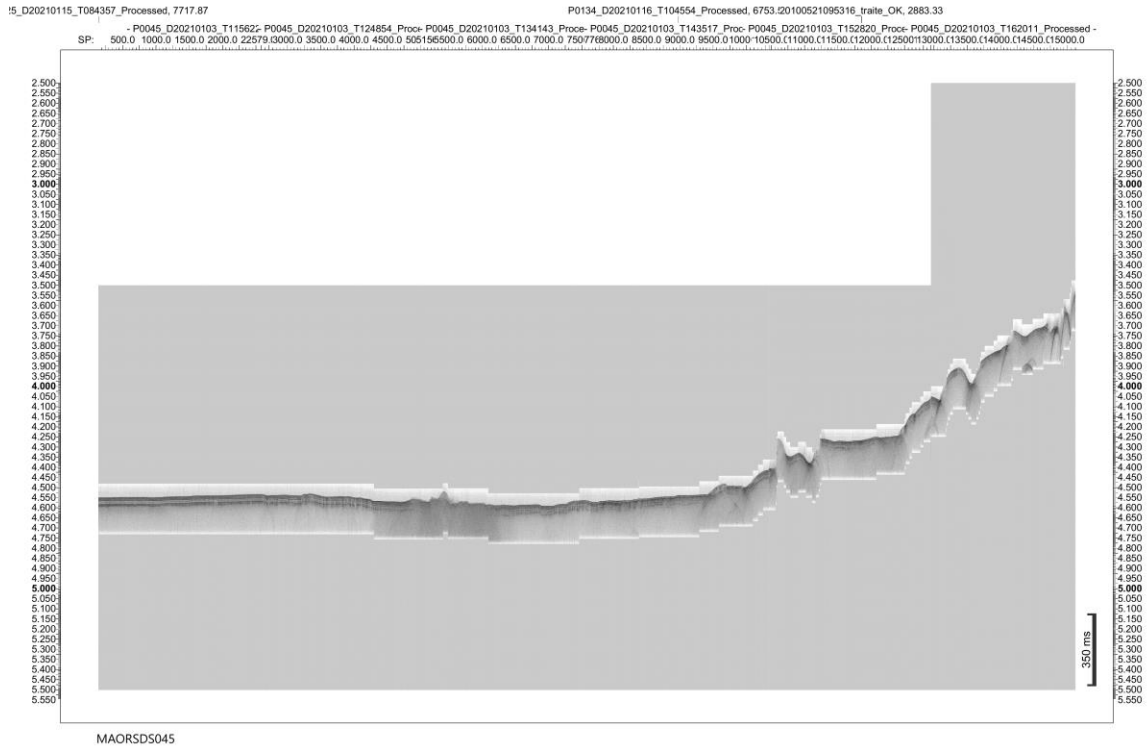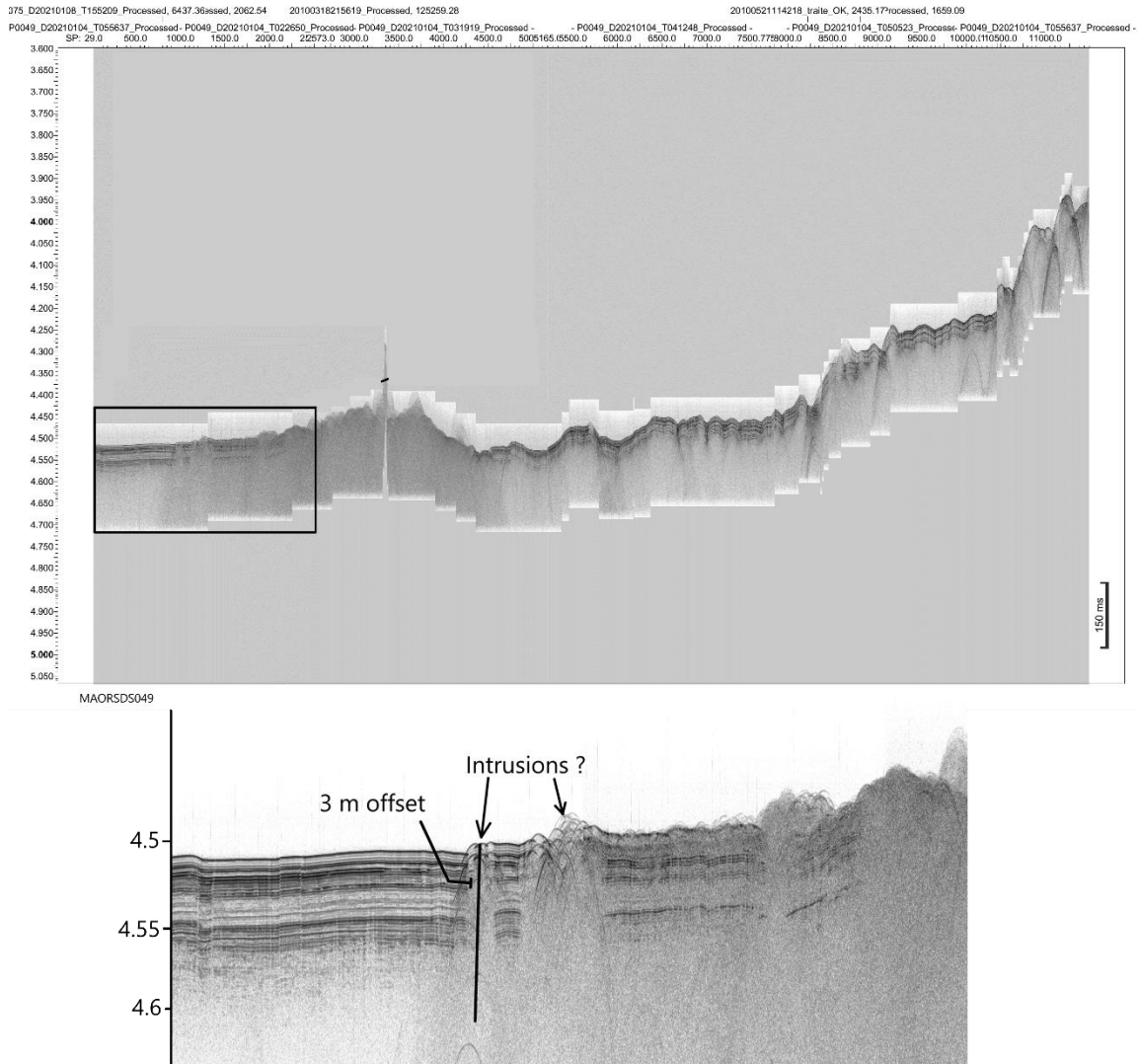**Figure S4-19:** NW-SE oriented uninterpreted sub-bottom profiler data MAORSDS070. Units as in Figure S4-2.
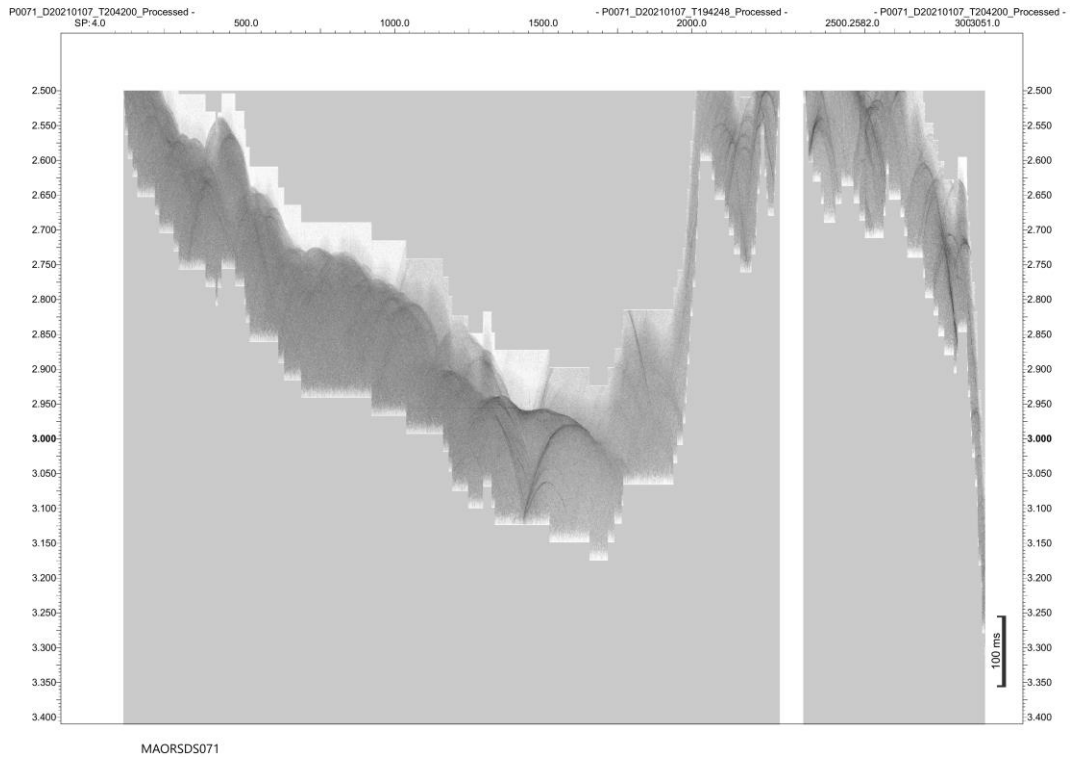
Figure S4-20: S-N oriented uninterpreted sub-bottom profiler data MAORSDS071. Units as in Figure S4-2.

Geochemistry, Geophysics, Geosystems
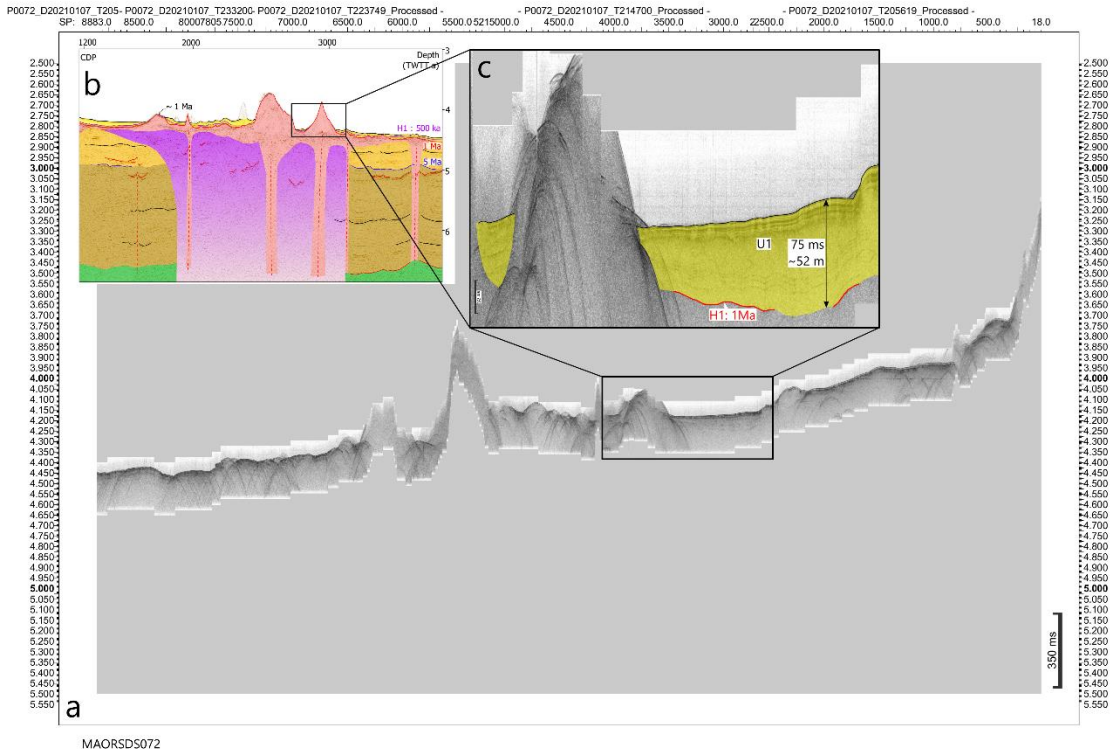
MAORSDS072

Figure S4-21: a) NW-SE oriented uninterpreted sub-bottom profiler data MAORSDS072. Units as in Figure S4-2. b) interpreted seismic profile (MAOR072 - Fig S3-21) at the same location. Symbols and colors of the sedimentary units, seismic horizons and reflectors, volcanic products and tectonic structures as in figures 6 and 7 of the main text c) Zoom of NW-SE oriented interpreted sub-bottom profiler data along the same profile showing one edifice and the sediment pile in more detail. Symbol and colors as in Figure 8 of the main text. On the seismic profile (Figure S4-21b), this cone is sealed by the reflector Hi2 (1Ma, red line) and began to form before 1 Ma. By comparing the thickness of the sedimentary unit above Hi2 (yellow (U1) + orange (a part of U2) in the seismic profile b) and yellow in the sub-bottom profiler data c), we showed that the seismic horizon Hi2 (red line on b and c) is located at the base of the seismic unit having a high of low amplitude continuous facies with layered horizon (see Fig. S6-1) and separate this unit from the incoherent facies below. This Hi2 horizon can therefore be distinguished in all sub-bottom profiler data.

47
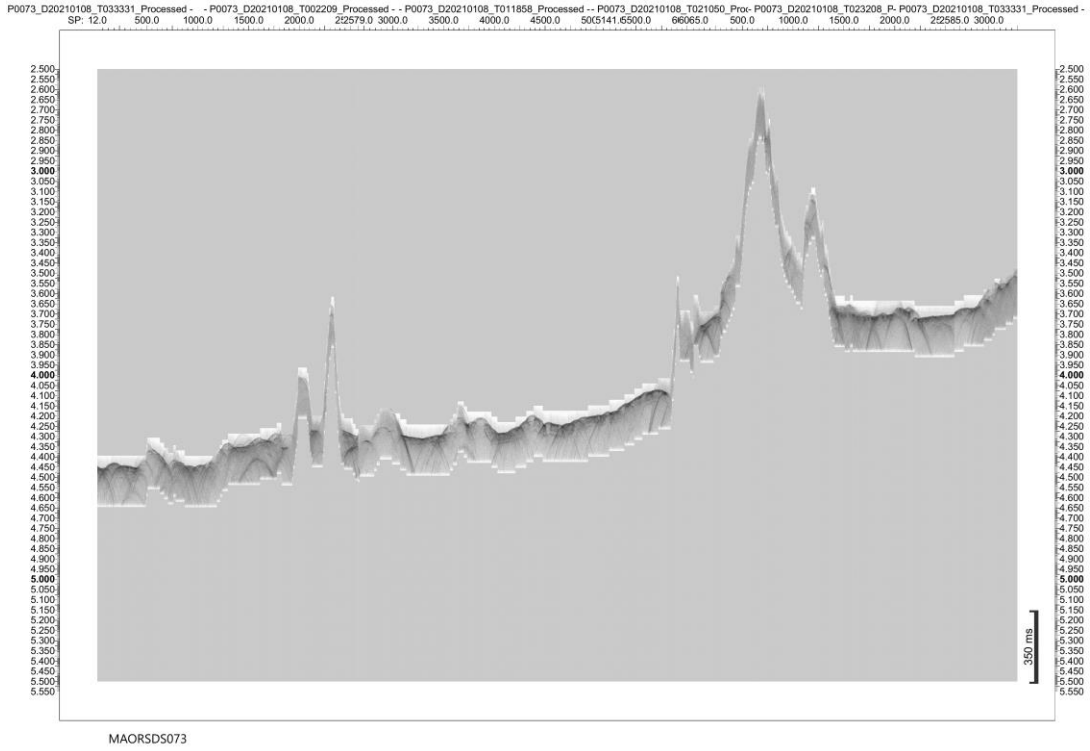
Figure S4-22: NE-SW oriented uninterpreted sub-bottom profiler data MAORSDS073. Units as in Figure S4-2.
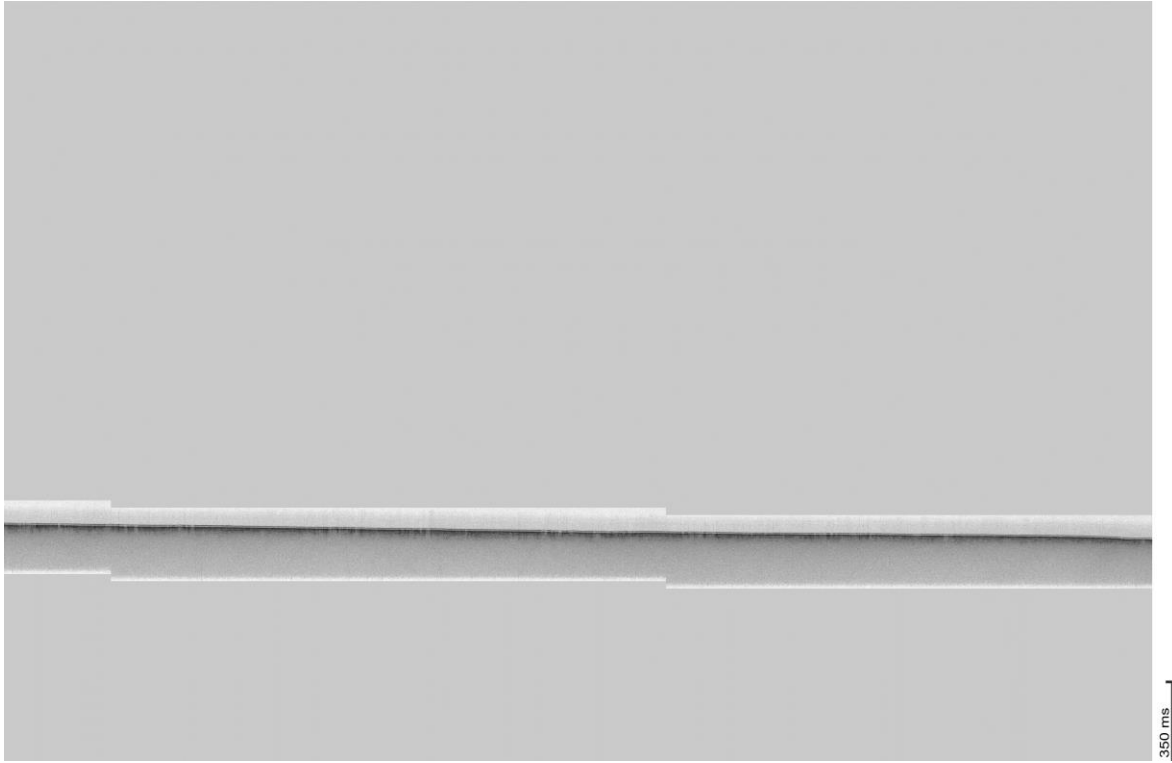
Figure S4-23: W-E oriented uninterpreted sub-bottom profiler data MAORSDS074. Units as in Figure S4-2.
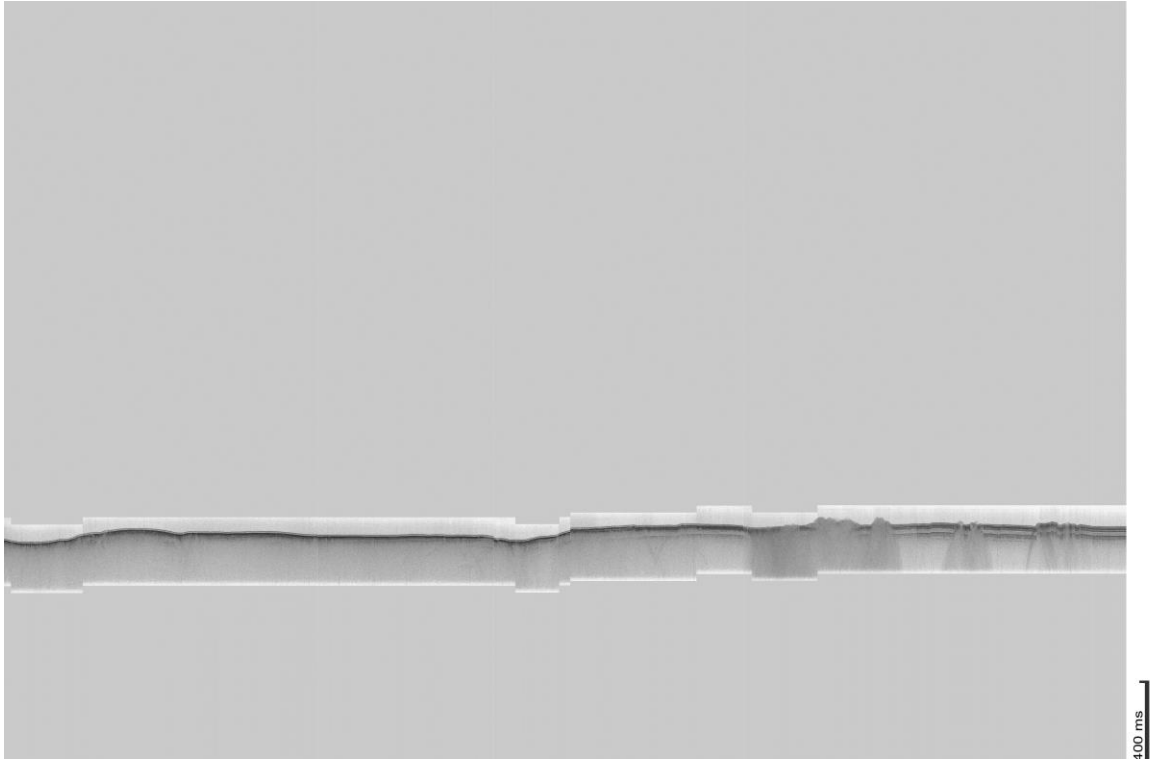
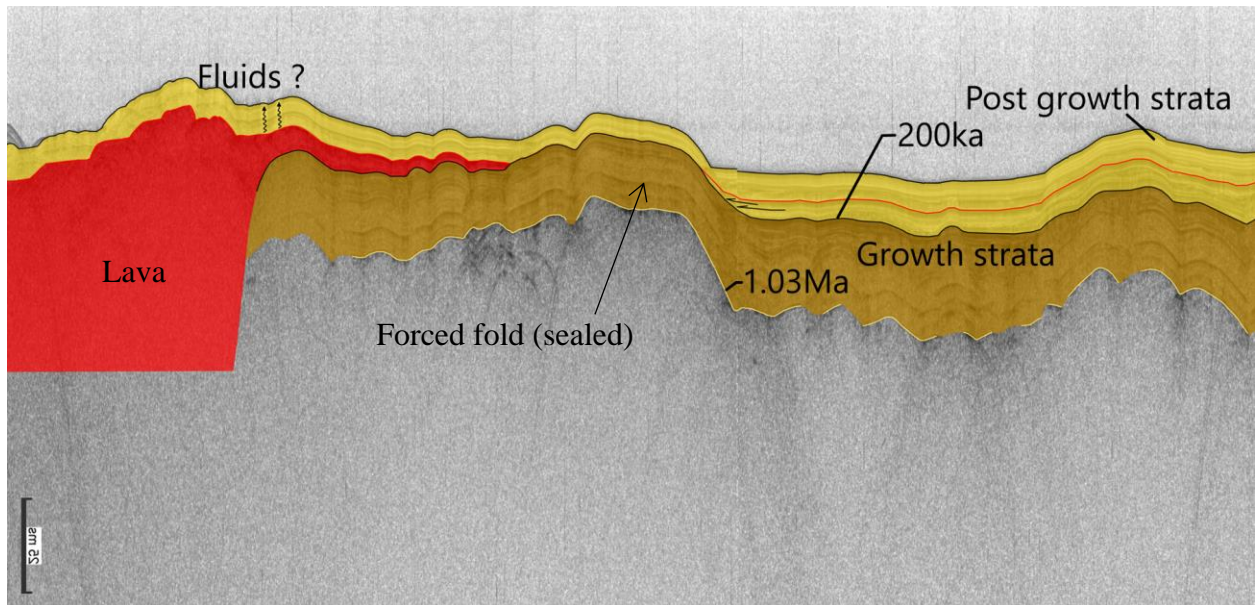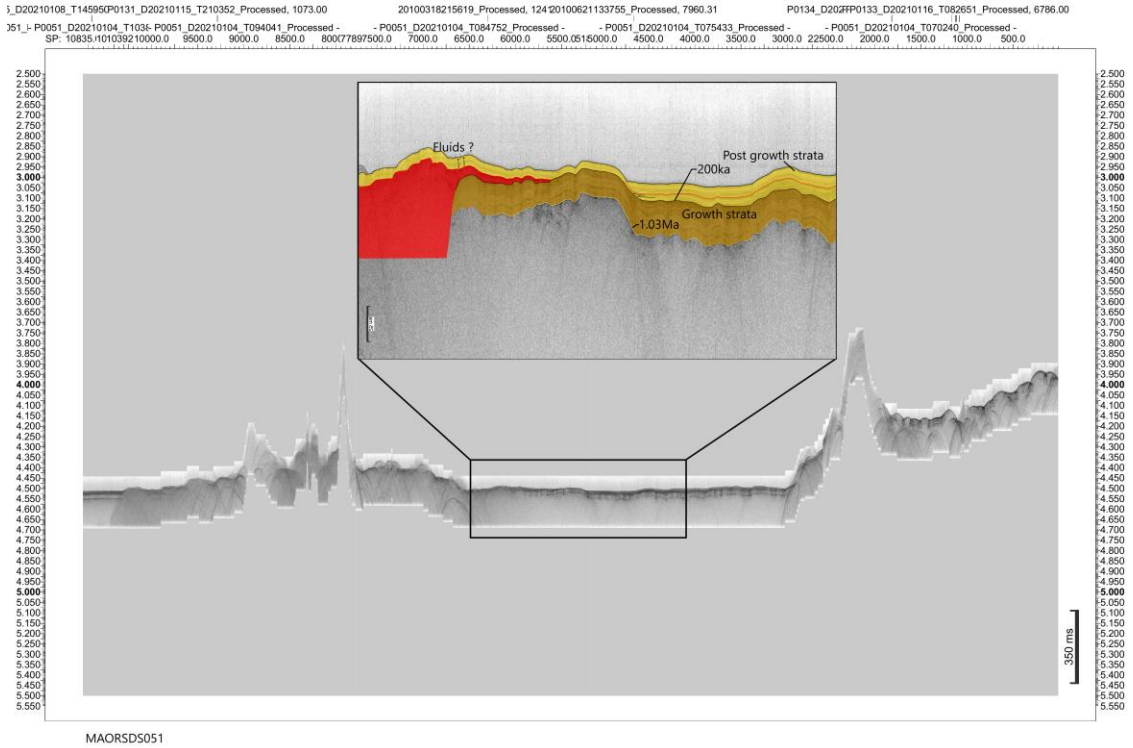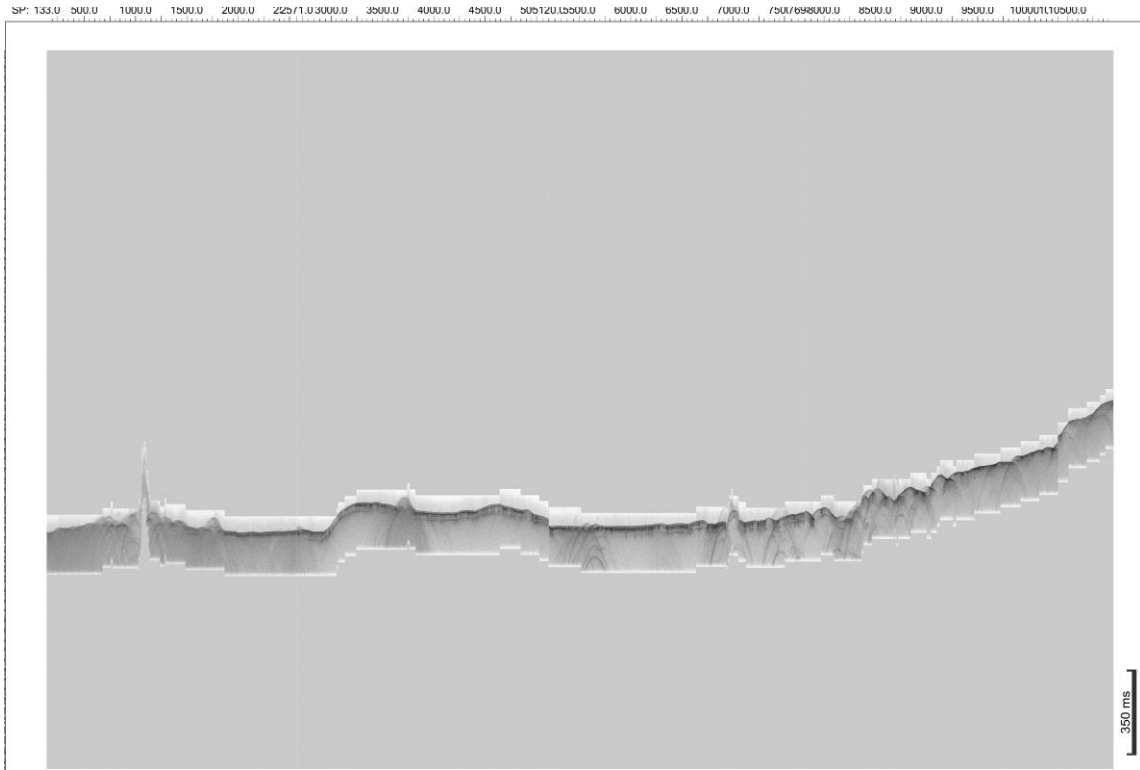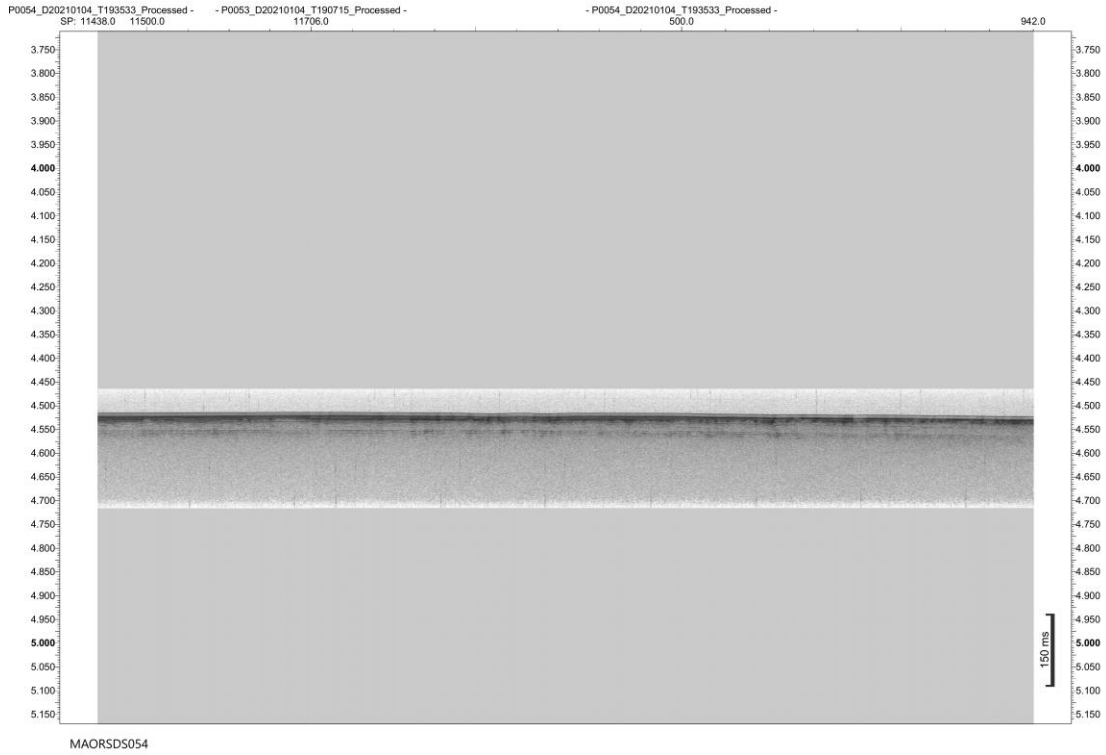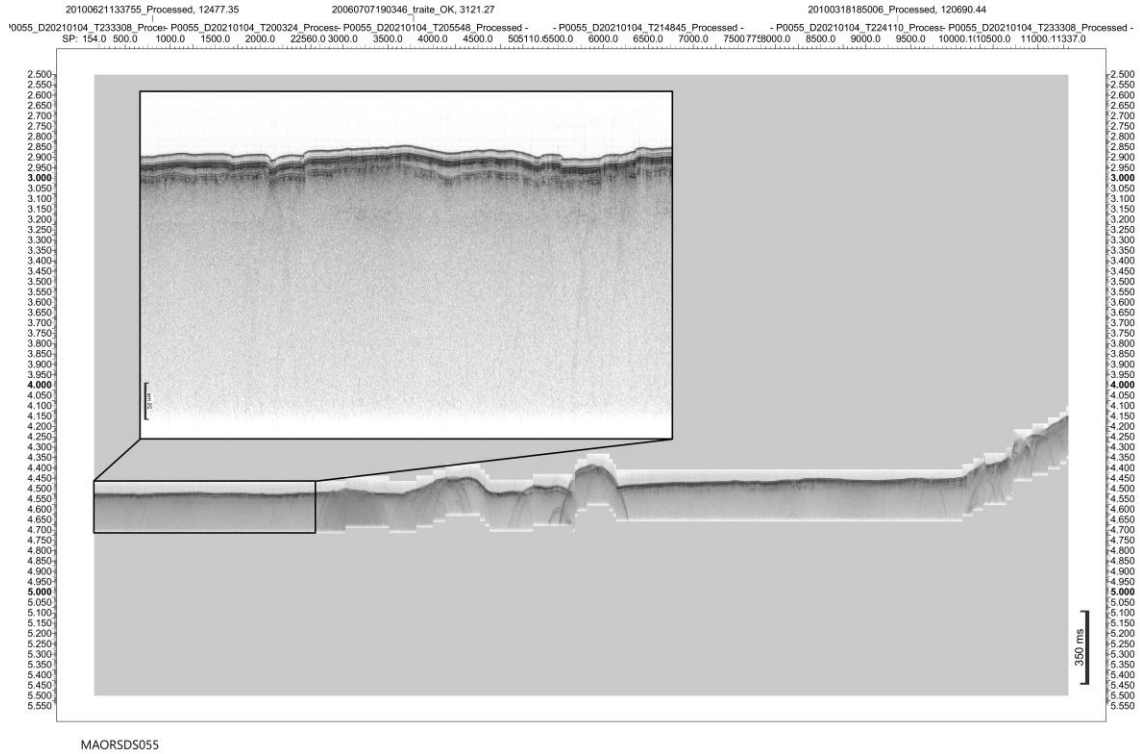**Figure S4-24:** NW-SE oriented uninterpreted sub-bottom profiler data MAORSDS075. Units as in Figure S4-2.
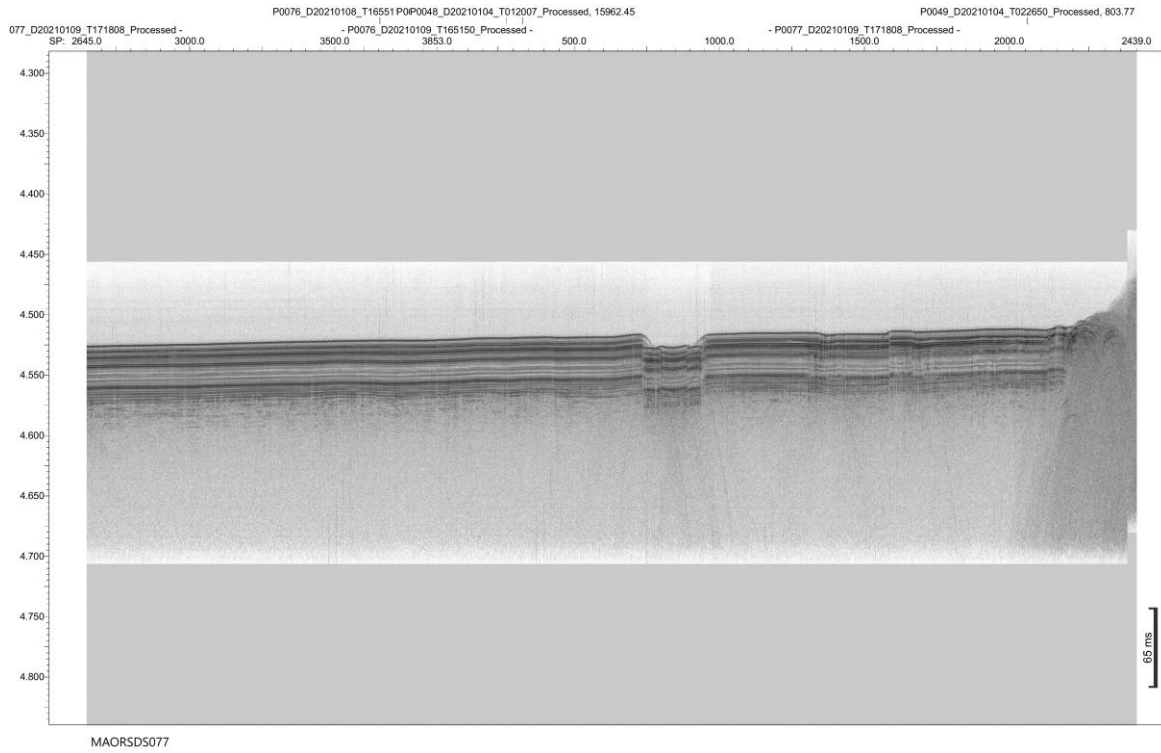
Figure S4-25: NW-SE oriented uninterpreted sub-bottom profiler data MAORSDS077. Units as in Figure S4-2.
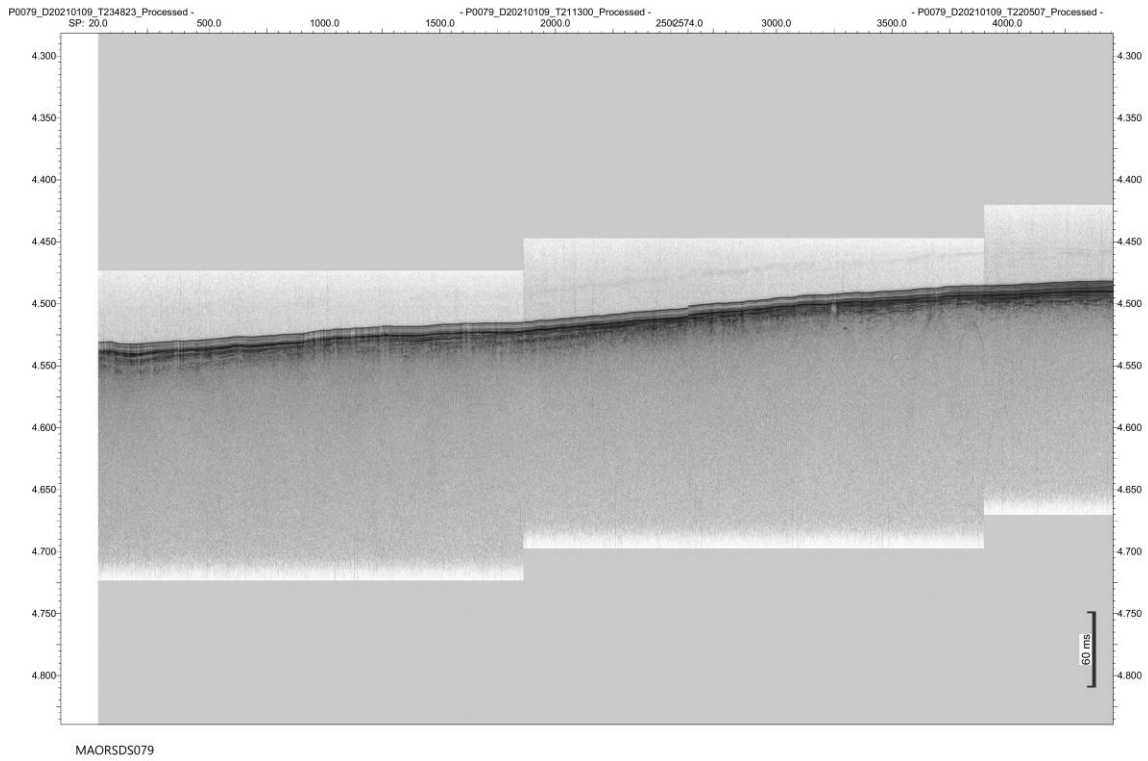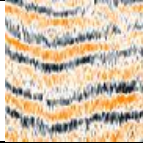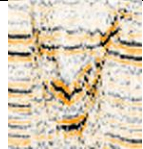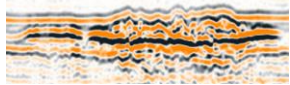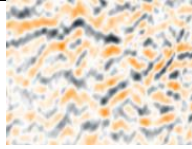
Figure S4-26: NW-SE oriented uninterpreted sub-bottom profiler data MAORSDS079. Units as in Figure S4-2.
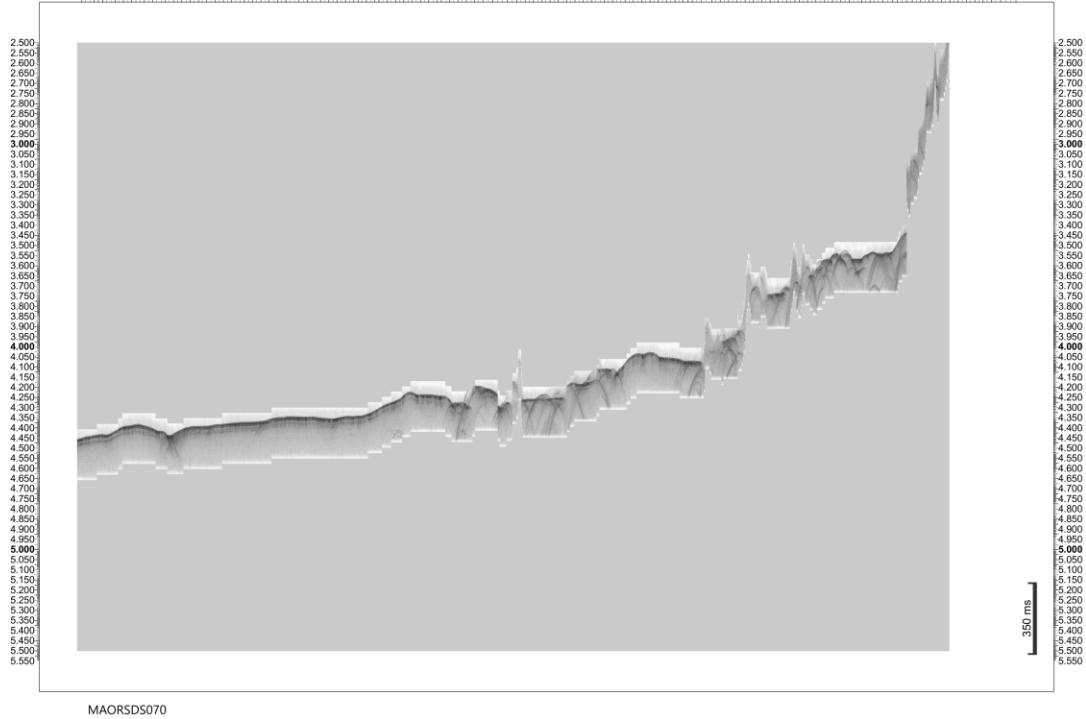
Supplementary material 5: Major seismic facies from the 48-channel reflection seismic profiles identified in the abyssal plain North of the Comoros archipelago.

Table S5-1: Major seismic facies and seismic units from the 48-channel reflection seismic profiles, identified into the sedimentary cover between the seafloor and the acoustic basement (Us). The seismic interpretation of the 48-channel seismic reflection profiles was based on the procedure defined by Mitchum et al. (1977)

Facies name	Continuity (Bad to good)	Amplitude (Low to high)	Frequency (Low to high) - Thickness max (ms)	Internal Reflection configuration	Example
U1 (50 ms max) Top of U1 corresponds to the seafloor; Base of U1 is the seismic horizon H1 (pink line) H1 is an unconformity, U1 onlaps U2					
F1	good	Medium	Medium to high - 10 - 15	Parallel	
U2 (250 - 300 ms max) Top of U2 is the seismic horizon H1 (pink line); Base of U2 is the seismic horizon H2 (purple line) H2 is a conform reflector, U2 onlap U3					
F2a	Low to good	high	Medium to high – 8 - 10	Parallel to subparallel	
F2b	Low to good	low	Medium to high - 8 - 10	Parallel to subparallel	
U3 (1750 ms max) Top of U3 is the seismic horizon H2 (purple line); Base of U3 is the horizon Hs, corresponding to the top of the acoustic basement Us (black line) HS is the top of the acoustic basement (red line)					

F3a	Low - good	Low - medium	Medium – 5 - 8	Parallel with local low angle oblique-parallel	
F3b	low - good	Low	Medium – 5 - 8	-	
Us Acoustic basement (deeper area, no reflective on the 48-channel seismic data)					
Fus	Good	Medium	High - 15	Parallel, locally oblique-parallel	
Facies of S-events					
Fs	Medium to high	High	-	Semi-chaotic to chaotic, often saucer-shaped	
Facies of lava flows					
Flava.1	No continuity good continuity of its base	Medium to high	Low	Heterogeneous, disrupted	
Flava.2 One reflector	High	High	Low	-	
Incoherent facies linked to volcanic blanking					
Fi	Low to no	Low to medium	Low to high	Weakly reflective Heterogeneous (continuous, chaotic) Outward and inward dipping	

Supplementary material 6: Sedimentary units and main seismic horizon in the 48-Channel seismic and sub-bottom profiler data for comparison.
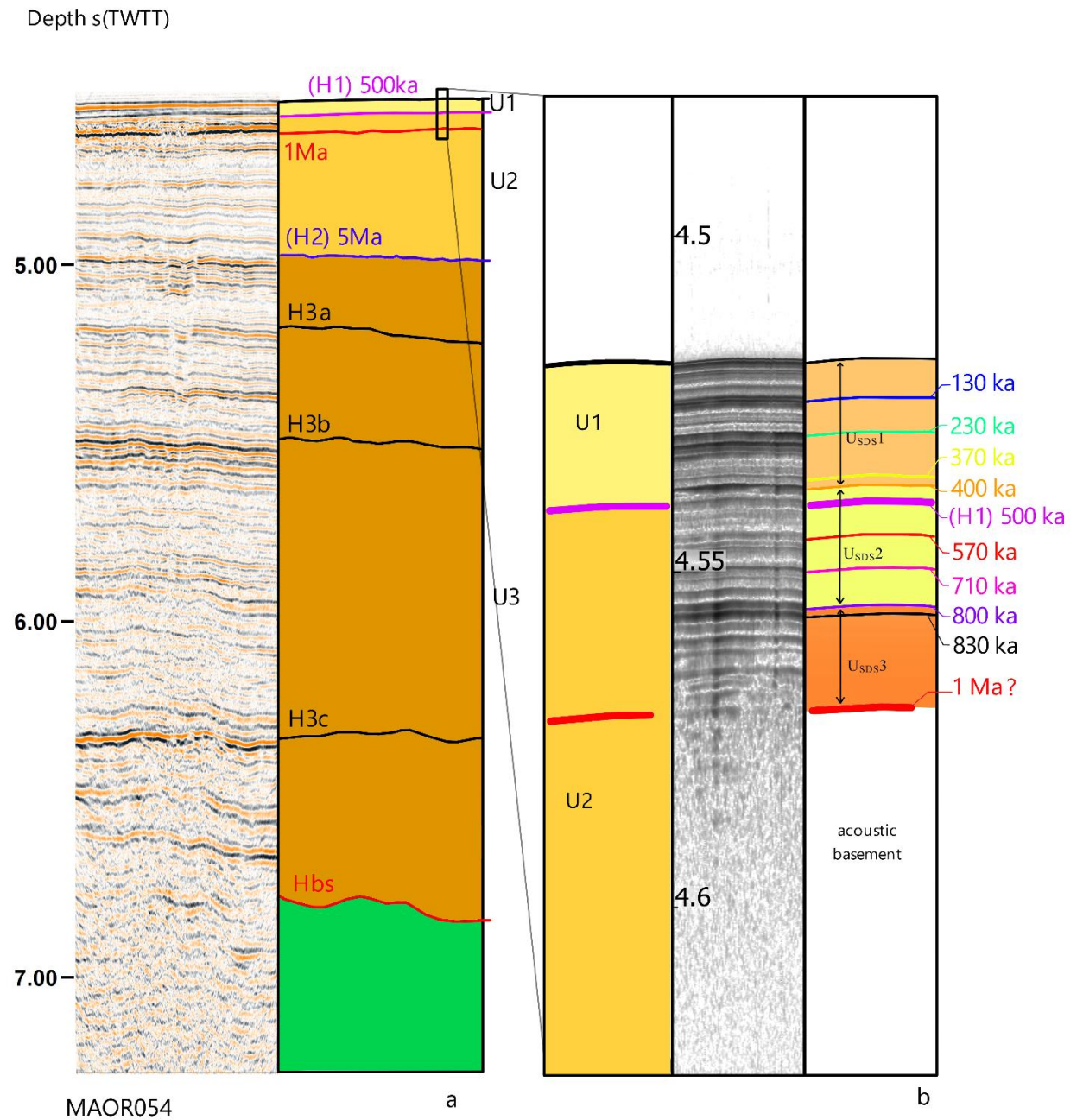
Figure S6-1: a) Logs of 48-channel seismic along the profile MAOR054, with main seismic horizons. The ages of the pink horizon (H1) 500ka, red horizon at 1Ma, the blue horizon at 5Ma in the 48-channel seismic reflection log were estimated from available sediment rates (Supplementary 7). Symbols and colors as in Figures 6 and 7 of the main text. b) Log the sub-bottom profiler at the same place (see location on a) showing the main sedimentary unit (central panel) of the 48 channels profile with main horizons with symbol and colors

as in a) (left panel), the main sedimentary units observed in the sub-bottom profiler. Colors and names of the units as log in Figure 8 Thick pink and red lines: main seismic horizon as in a. Thin colored lines: main seismic horizons identified in the sub-bottom profiler data. The horizons are correlated to the main dated sedimentary units observed in the cores MD21-3602 with ages (estimated from δO18 stratigraphy).

Supplementary material 7: Sedimentation rates
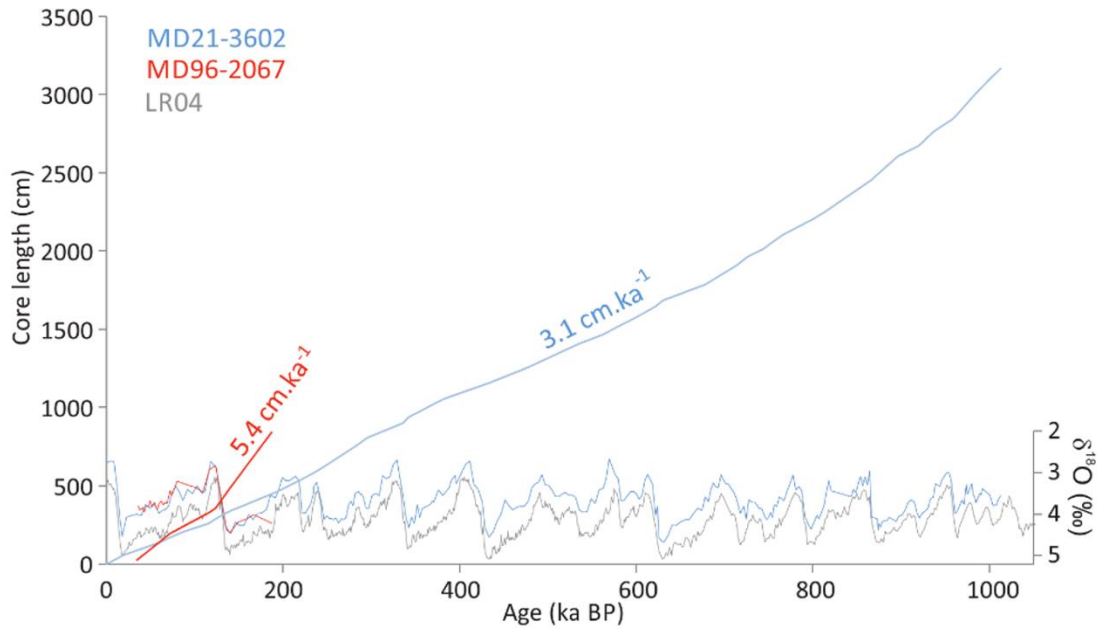
Figure S7-1 (b) Mean sedimentation rates estimated from δO18 stratigraphy for the cores MD96-2067 (21.5m-long) and MD21-3602 (32m-long) acquired during the MOZAPHARE (Lancelot, 1996) and SCRATCH (Berthod et al., 2022) marine cruises (Location of cores in Figure 2 of the main text). Oxygen isotopic stratigraphy indicate sedimentation rates of ~5.4 cm/ka and 3.1 cm/ka for the hemipelagic section of the cores at the MD96-2067 and MD21-3602 sites, over the last 200 and 1000 ka, respectively.

Supplementary material 8: Mechanical model of the dyke swarms in MWEZI.

In the western part of the Mwezi volcanic field (the M3 subarea in Figure 11.a), we identified an impressive set of radial dykes with wide range of orientations from N110°E to N45°E, and originating from central subarea M2. Dyke swarms' patterns have been used as markers of the ambient stress field, in various volcanic zones worldwide; in Colorado (Odé et al., 1957, Muller and Pollard, 1977), in the Galapagos (Chadwick and Howard, 1991), in East Antarctica (Hoek et al., 1995) and more recently around the Alba Patera Martian volcano (Cailleau et al., 2003). Odé et al. (1957) showed that dyke propagation in the sedimentary cover is directly controlled by the ambient stress field as the dyke plan progresses orthogonally to the smallest compressive stress σ_3.. The presence of the radial set in Mwezi suggests a local stress perturbation of the regional stress field.

Analog radial dyke swarms were observed and described elsewhere departing from volcanic edifices (Hou et al., 2012, Cailleau et al., 2003, Chadwick et al., 1990, Paquet et al., 1997). These authors suggest that the topography controls the swarm distribution. It's worth nothing that our radial dyke swarm is the identified on a flat seafloor (around 3400m), the other analogues having been often observed in area of contrasting topography (Acocella and Neri, 2018).

From our observations, the orientation of the dyke swarm may result from the interplay between tectonic and/or magmatic processes. To test this, we created a simple 2D numerical model of uniform regional stress field locally disrupted in all directions by a circular point source (a magma chamber).

The parameters for the uniform regional stress field and circular source were calibrated with the least square method to find the ambient stress field that best fits the orientations of the dikes of the M3 subarea. The resulting stress field is an N40°E oriented regional extension with the local circular disruption (magma chamber) localized in Mwezi province M2 area (numbered 1 in Figure 12 of the Main text).

I Method

I.1 The stress field model

We established a stress field model by superposing a regional, uniform stress field to one generated by a local axisymetric radial stress field resulting from a pressurized cylindrical intrusion. The proposed model was adapted from the model of Baer et Reches, 1991 from the work of Muller et al, 1977 and Odé et al, 1957.

First, we consider the stress field generated around a cylindrical magmatic source that depends of the radius of the source r_0 and the pressure P. The stresses (Figure III. A) defined in the polar coordinate system centered around the center of the magmatic chamber are:

$$\begin{cases} \left(\sigma_r(r,\theta)\right)_{loc} = -\left(\sigma_\theta(r,\theta)\right)_{loc} = \dfrac{P r_0{}^2}{r^2} & (1) \\ \left(\tau(r,\theta)\right)_{loc} = 0 \end{cases}$$

In addition, we consider a homogeneous regional 2-dimensional stress field defined by its maximal and minimal principal stress direction (σ1)reg and (σ3)reg respectively. The orientation of the stress field is defined by the angle Φ between the major principal stress direction and $\overrightarrow{u_x}$, the horizontal axis in the cartesian coordinate system. The stresses (Figure III. A) in the polar coordinate system centered around the center of the magmatic chamber are:

$$
\begin{cases}
\left(\sigma_r(r,\theta)\right)_{reg} = (\sigma_3)_{reg} + \left((\sigma_1)_{reg} - (\sigma_3)_{reg}\right)\cos^2(\theta - \phi) \\
\left(\sigma_\theta(r,\theta)\right)_{reg} = (\sigma_3)_{reg} + \left((\sigma_1)_{reg} - (\sigma_3)_{reg}\right)\sin^2(\theta - \phi) \quad (2) \\
\left(\tau(r,\theta)\right)_{reg} = -\left((\sigma_1)_{reg} - (\sigma_3)_{reg}\right)\sin(\theta - \phi)\cos(\theta - \phi)
\end{cases}
$$

Finally, the stress field resulting from the superposition of (1) and (2) is defined as:

$$
\begin{cases}
\sigma_r(r,\theta) = \dfrac{P r_0^2}{r^2} + (\sigma_3)_{reg} + \left((\sigma_1)_{reg} - (\sigma_3)_{reg}\right)\cos^2(\theta - \phi) \\
\sigma_\theta(r,\theta) = -\dfrac{P r_0^2}{r^2} + (\sigma_3)_{reg} + \left((\sigma_1)_{reg} - (\sigma_3)_{reg}\right)\sin^2(\theta - \phi) \quad (3) \\
\tau(r,\theta) = -\left((\sigma_1)_{reg} - (\sigma_3)_{reg}\right)\sin(\theta - \phi)\cos(\theta - \phi)
\end{cases}
$$

Where α the angle between the local major principal stress direction and the radial direction from the source (Figure III. A) is defined by:

$$
\tan 2\alpha = \frac{2\tau(r,\theta)}{\sigma_r(r,\theta) - \sigma_\theta(r,\theta)} \quad (4)
$$

Combining (3) and (4) α can then be defined as:

$$
\alpha(r,\theta) = \frac{1}{2}\arctan\left(\frac{-A}{\dfrac{r_0^2}{r^2} + \dfrac{A}{2}\left(\cos^2(\theta - \phi) - \sin^2(\theta - \phi)\right)}\right) \quad (5)
$$

$$\text{Where: } A = \frac{(\sigma_1)_{reg} - (\sigma_3)_{reg}}{P}$$

Since α marks the angle between the major principal stress direction at a point (r,θ) and the radial direction, the angle $\omega(r,\theta) = \alpha(r,\theta) + \theta$ is used to orientate the resulting stress field in the cartesian coordinates (Figure III. A).

The calculated stress trajectory map depends on only a few unknown parameters:

- r_0 , the radius of the magmatic chamber
- ϕ the angle between the major principal regional stress direction $(\sigma_1)_{reg}$ and the horizontal axis $\overrightarrow{u_X}$ (Figure III. A).
- $A = \frac{(\sigma_1)_{reg} - (\sigma_3)_{reg}}{P}$ the normalized tectonic shear stress.

The precise tx and ty location of the magmatic perturbation is not known. Thus, equation (5) is modified to include the tx and ty parameters:

- r_0 is the radius of the magma chamber.

- ϕ corresponds to the angle of the horizontal axis $\overrightarrow{u_X}$ with a principal stress of the regional homogeneous stress field.

- *A* is a ratio used to describe the relative strength of the local magmatically

  driven stress field with the regional homogeneous stress field.

$$\omega(r,\theta) = \frac{1}{2} arctan\left(\frac{-A\,sin(\theta_t - \phi)\,cos(\theta_t - \phi)}{\frac{r_0{}^2}{r_t{}^2} + \frac{A}{2}\left(cos^2(\theta_t - \phi) - sin^2(\theta_t - \phi)\right)}\right) + \theta_t \quad (6)$$

Where: $A = \frac{(\sigma_1)_{reg} - (\sigma_3)_{reg}}{P}$

And $\begin{cases} \theta_t = arctan2(r \times sin\,\theta - t_Y, r \times cos\,\theta - t_X) \\ r_t = \sqrt{(r \times sin\,\theta - t_Y)^2 + (r \times cos\,\theta - t_X)^2} \end{cases}$

I.2 Fitting the stress field to the ground truth

The orientation of a dyke is a marker of the local stress field and is used as ground truth to which we fit the superposed stress field. We define ω(r,θ) to characterize the local dyke orientation. ω varies along a dyke.

As such, the goal here is to find the best parameters r_0, φ, A, t_X and t_Y that produce a resulting stress field that best fits the orientation of the dykes. Or, in mathematical terms:

$\hat{X} = (r_0, \phi, A, t_X, t_Y)^T$ the vectors of the parameters the stress field depends upon

$Y_{obs} = \left(\omega(r,\theta)_{0_{obs}}, \dots, \omega(r,\theta)_{i_{obs}}, \dots, \omega(r,\theta)_{n_{obs}}\right)^T$ the vector compiling the values of ω along every dyke of the North-western part of the Mwezi volcanic province.

$Y_{mod} = \left(\omega(r,\theta)_{0_{X,mod}}, \dots, \omega(r,\theta)_{i_{X,mod}}, \dots, \omega(r,\theta)_{n_{X,mod}}\right)^T$ the vector compiling the angles ω computed for the stress field described by the parameters in X. The angles ω are computed for the same (r, θ) positions as for the angles of vector Y_{obs}.

As such, this problem aims at minimising the quadratic sum of the residual values of the vector R defined by: $R = Y_{obs} - Y_{mod}$
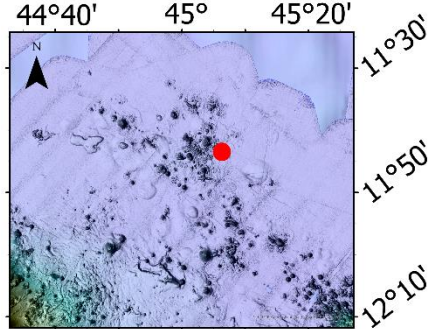
To do so, a least square method is used to find the set of parameters X that best approximates the data.

II Results

Depending on the geological data we use as ground truth to fit the regional superimposed stress field, the results can vary:

- Figure S8-2 shows the results obtained by using only the Northwestern dyke

    swarm to the West of M1:

Table S8-1: Set of parameters that describes the superimposed (to the regional stress) local stress field that best fits the pattern of dyke swarm of the M3 sub-area of Mwezi.

r_0	ϕ	A	Localization of the center of the magmatic perturbation (t_X, t_Y)
2.3 km	25.1 ° (=N65)	0.02	

- Figure S8-3 corresponds to the results obtained with the dyke swarm in M3

    sub-area 3 and the volcano-tectonic structural alignments in M2 subarea

Table S8-2: Set of parameters that describe the superimposed (to the regional stress) local stress field that best fits the dyke swarm and volcanic alignments of the M3 and M2 area.
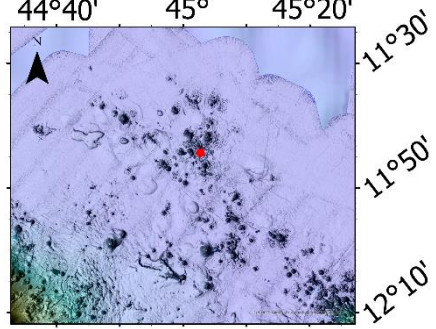
r_0	ϕ	A	Localization of the center of the magmatic perturbation (t_X, t_Y)
1 km	50.8 ° (=N40.2)	0.001	

Figure S8-2 and S8-3 show that, in both cases, the northwestern part of the dyke swarm fits the model with accuracy. This observation is particularly true in the Northwestern corner of the volcanic field where the dyke network aligns with the principal stresses of the model.

The parameters of the local perturbation, meaning its radius (r_0) and its position in the volcanic field (t_X, t_Y), describe a disturbance of 2 to 4 km in diameter located at the center of the Mwezi volcanic field. This observation remains fairly consistent based on whether we use only the dykes or the dykes in conjunction with the surface structural alinements for the calibration. Considering the high presence of volcanic cones and sills in this portion of the Mwezi volcanic field. The stress field perturbation described here could be of magmatic origin.

The regional stress field is characterized by its orientation (Φ). Here we see variation for this parameter based on whether we only use dyke alinements for the model's calibration or use them in conjunction with the other structural alinements. On the one hand, if only the dyke swarm is used, the minimal principal stress component is oriented N65. On the other hand, if both datasets are used, it is oriented N45. This difference of 20 degrees is significant. However, this could be linked to the inherent bias of our method of inferring the path of the dykes. In fact, we are limited to only mapping the dykes that both appear in seismic reflection profiles and are topped with a graben structure that can be followed in bathymetry. We only map a fraction of the dyke swarm. Most of mapped dykes are in the Northern and North-western part of the Mwezi volcanic province and dykes that cannot be mapped in the rest of the field are not considered. The dykes of this Northern/North-western part of the volcanic field are overrepresented and given too much weight in the calibration of the stress field. Including surface volcano-tectonic structures in conjunction to the dykes can help mitigate this effect even if those structures emplacements might not be controlled by the local stress regime exclusively. Moreover, differences between observed field data and the model might also come from the assumption we made of a uniform stress field in a linearly isotropic medium. There is no consideration of potential heterogeneities (faults/fractures, previous intrusions, lithologies, …).

Overall, the results show that the regional stress had an influence during the settlement of the dyke swarm. Otherwise, the dyke swarm would be radially distributed around the source. One can note that some structures do not align with the direction predicted by the model. This could be due to the model assumptions: a uniform stress field in a linear elastic isotropic medium. Dykes can propagate along inherited heterogeneities (faults and fractures change in lithology, …) (Reynolds et al, 2017).
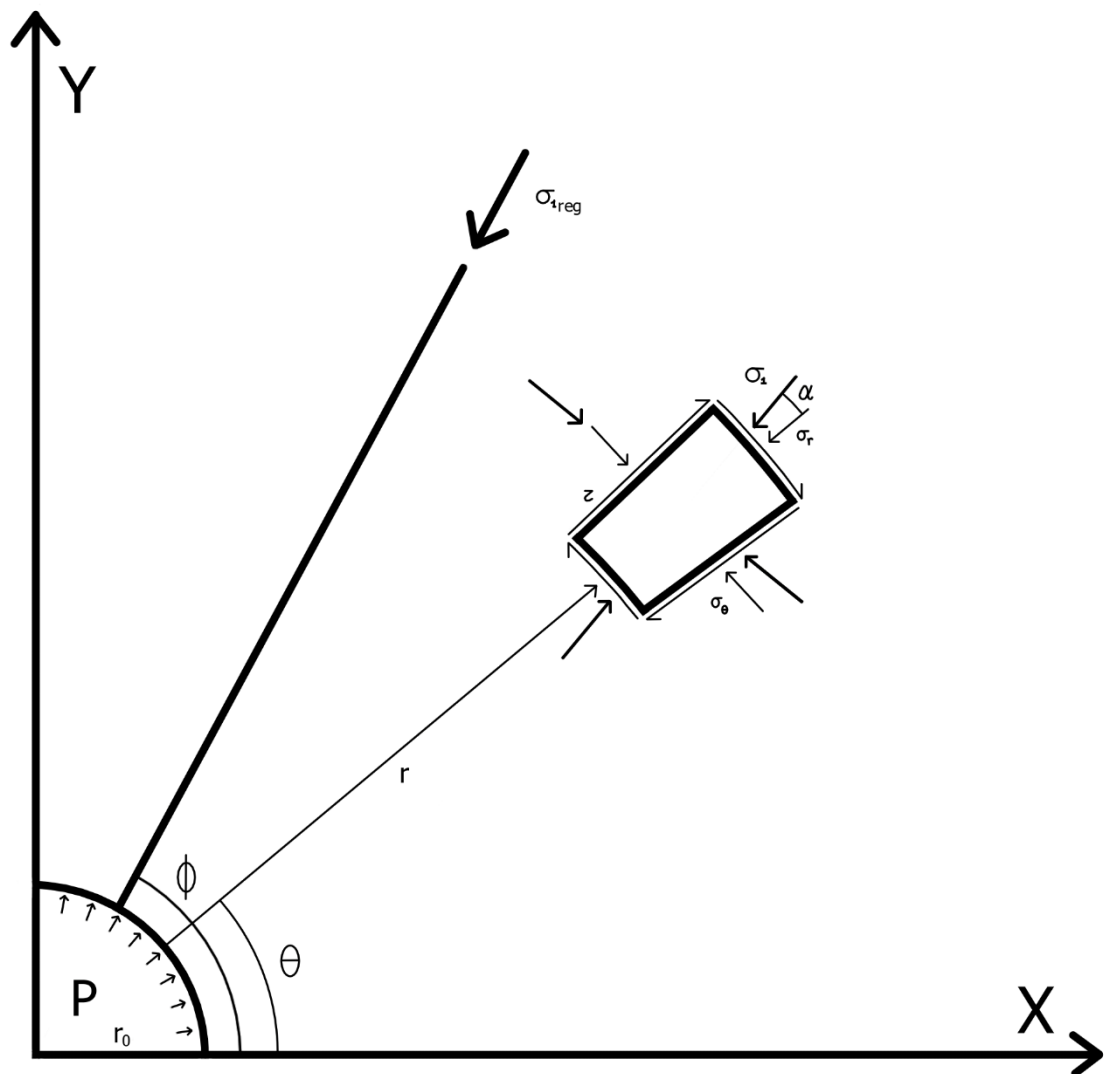
Figure S8-1: Maximal principal stresses for a regional homogeneously oriented stress field, for a radial stress field generated by a spheric magmatic chamber and for the stress field resulting from the superposition of the two former ones. Adapted from Baer et Reeches: 1991.
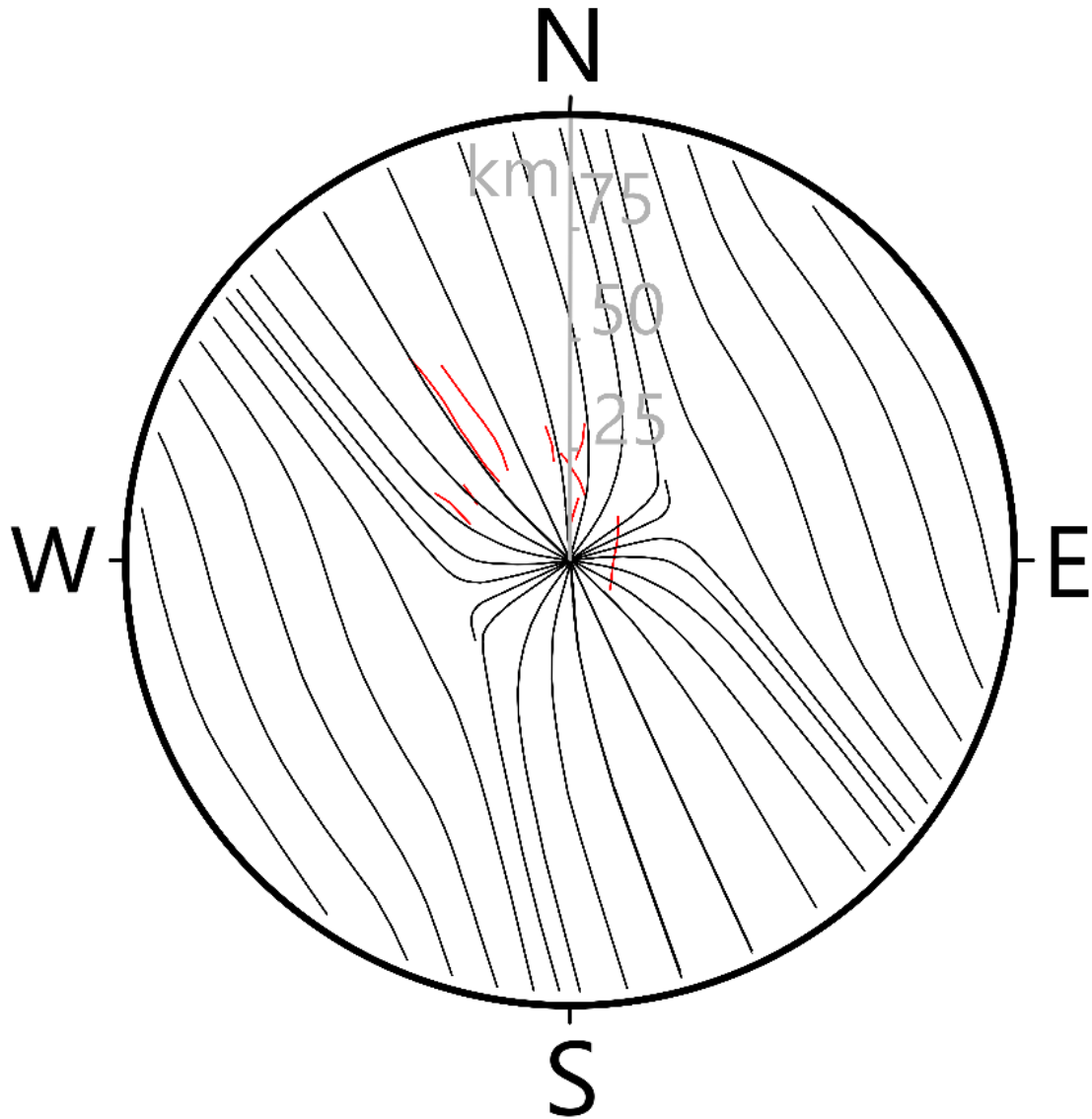
Figure S8-2: Best fitted stress field on the dykes' measured orientations. Fitted parameters used to characterize the stress field are: tx = 10.0 km, ty = 0.0 km, ϕ = 25.1°, r_0 = 2.3 km and A = 0.021
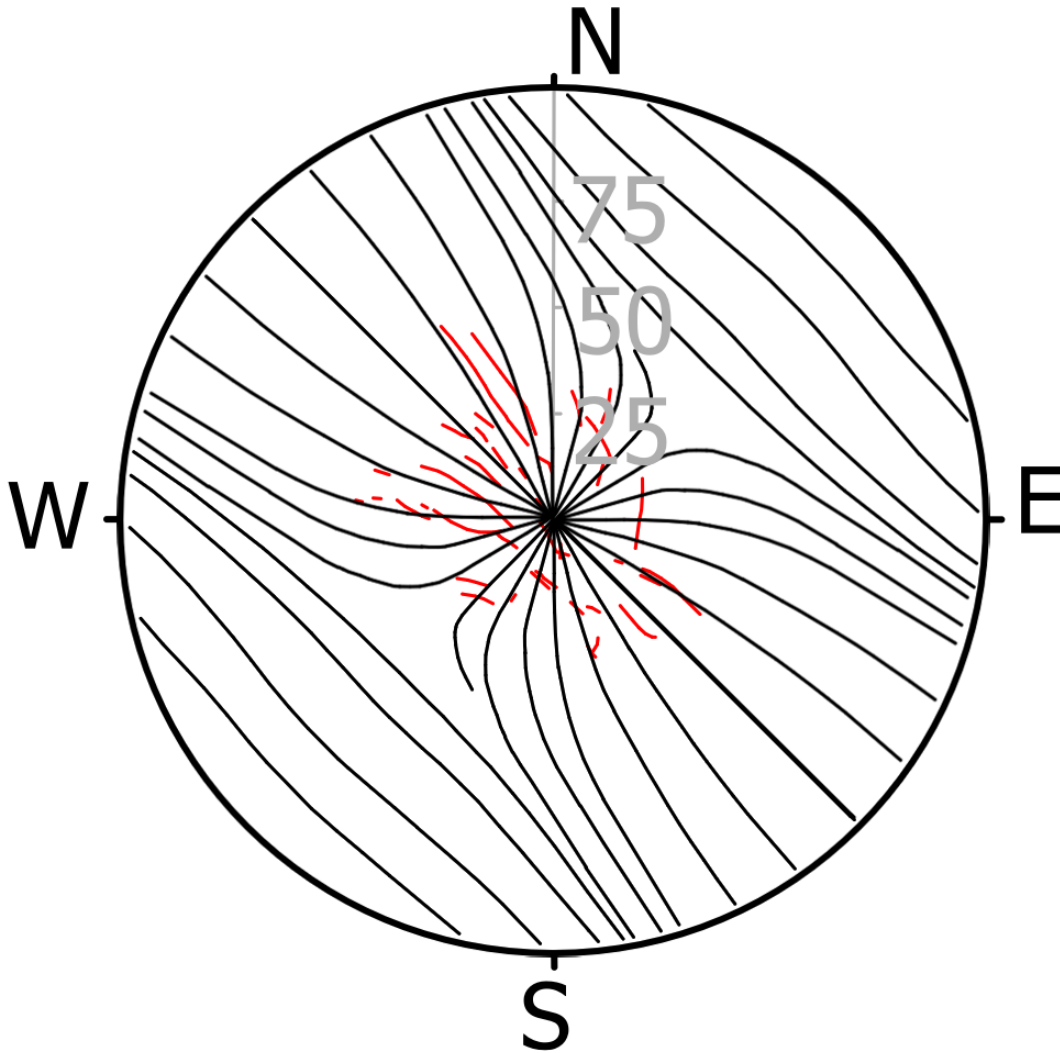
Figure S8-3: Best fitted stress field on the dykes' and other volcano tectonic structures' measured orientations. Fitted parameters used to characterize the stress field are: tx = 0.0 km, ty = 0.0 km, ϕ = 40.8°, r_0 = 1 km and A = 0.021
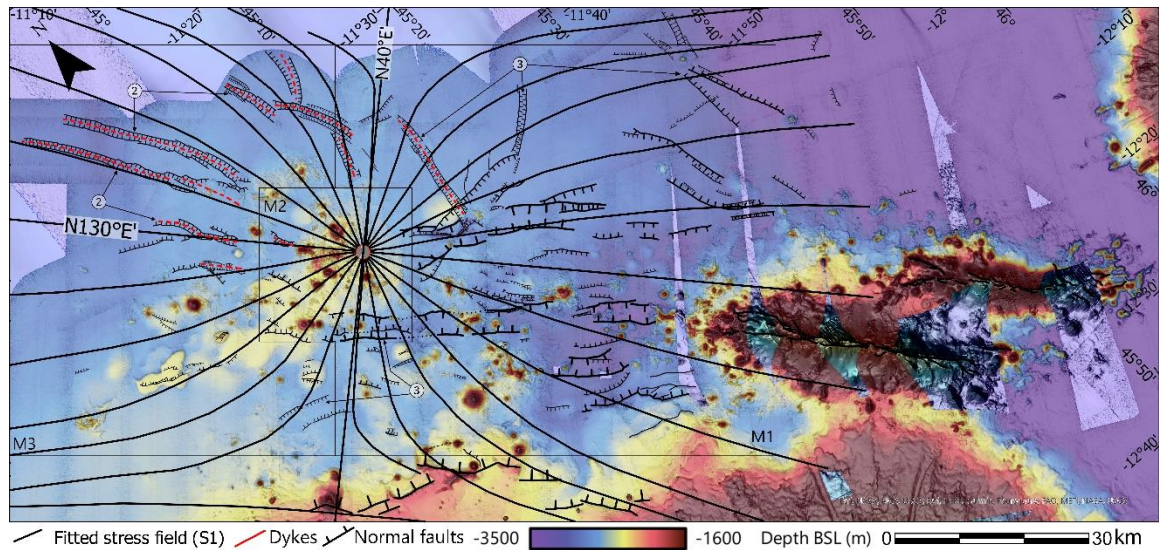
Figure S8-4. Comparison between the modelled pattern of dikes induced by superimposed local (volcanic source) and regional (N40°E extension) to the geological observations in the Mwezi-Jumelles province. Bathymetry, faults and dikes as in Figure 11 of the main text. The ambient stress field results from an uniform regional stress field (N40°E regional extension) superimposed with a local stress field (circular source , i.e. a magma chamber), located in Mwezi province M2 area (numbered 1). Black lines as in Figures S3-2 and 8. The orientation of the modelled dykes fits with the orientation of normal faults and dikes below (numbered 2) in the M3 sub-area, but not with that of faults in the M1 area (particularly that numbered 3). We infer that the local source of perturbation is assymetric; acting on one side of the model as expected at the tip of a propagating crack (see main text)